THE *HUBBLE SPACE TELESCOPE* TREASURY PROGRAM ON THE ORION NEBULA CLUSTER[*],[†]

M. ROBBERTO[1], D. R. SODERBLOM[1], E. BERGERON[1], V. KOZHURINA-PLATAIS[1], R. B. MAKIDON[1], P. R. MCCULLOUGH[1],
M. MCMASTER[1], N. PANAGIA[1,2], I. N. REID[1], Z. LEVAY[1], L. FRATTARE[1], N. DA RIO[3], M. ANDERSEN[3], C. R. O'DELL[4],
K. G. STASSUN[4,5,6], M. SIMON[7], E. D. FEIGELSON[8], J. R. STAUFFER[9], M. MEYER[10], M. REGGIANI[10], J. KRIST[11],
C. F. MANARA[12], M. ROMANIELLO[12], L. A. HILLENBRAND[13], L. RICCI[13], F. PALLA[14], J. R. NAJITA[15], T. T. ANANNA[16],
G. SCANDARIATO[2], AND K. SMITH[17]

[1] Space Telescope Science Institute, 3700 San Martin Drive, Baltimore, MD 21218, USA; robberto@stsci.edu
[2] INAF-CT Osservatorio Astrofisico di Catania, Via S. Sofia 79, I-95123 Catania, Italy
[3] European Space Agency, Keplerlaan 1, 2200-AG Noordwijk, The Netherlands
[4] Department of Physics and Astronomy, Vanderbilt University, 6301 Stevenson Center, Nashville, TN 37235, USA
[5] Department of Physics, Fisk University, 1000 17th Ave. N., Nashville, TN 37208, USA
[6] Department of Physics, Massachusetts Institute of Technology, 77 Massachusetts Ave., Cambridge, MA 02139, USA
[7] Department of Physics and Astronomy, Stony Brook University, Stony Brook, NY 11794, USA
[8] Department of Astronomy and Astrophysics, Pennsylvania State University, 518 Davey Lab, University Park, PA 16802, USA
[9] Spitzer Science Center, California Institute of Technology 314-6, Pasadena, CA 91125, USA
[10] ETH Zürich, Institut für Astronomie, Wolfgang-Pauli-Strasse 27, CH-8093 Zürich, Switzerland
[11] Jet Propulsion Laboratory, California Institute of Technology, 4800 Oak Grove Drive, Pasadena, CA 91109, USA
[12] European Southern Observatory, Karl-Schwarzschild-Strasse 2, D-85748 Garching, Germany
[13] Cahill Center for Astronomy and Astrophysics, California Institute of Technology, 1200 East California Boulevard, Pasadena, CA 91125, USA
[14] INAF-Osservatorio Astrofisico di Arcetri, Largo Enrico Fermi 5, I-50125 Firenze, Italy
[15] National Optical Astronomy Observatories, 950 N. Cherry Ave, Tucson, AZ 85719, USA
[16] Bryn Mawr College, 101 North Merion Avenue, Bryn Mawr, PA 19010, USA
[17] Max Planck Institut für Astronomie, Königstuhl 17, D-69117 Heidelberg, Germany

ABSTRACT

The *Hubble Space Telescope (HST)* Treasury Program on the Orion Nebula Cluster (ONC) has used 104 orbits of *HST* time to image the Great Orion Nebula region with the Advanced Camera for Surveys (ACS), the Wide-Field/ Planetary Camera 2 (WFPC2), and the Near-Infrared Camera and Multi-Object Spectrograph (NICMOS) instrument in 11 filters ranging from the *U* band to the *H* band equivalent of *HST*. The program has been intended to perform the definitive study of the stellar component of the ONC at visible wavelengths, addressing key questions like the cluster initial mass function, age spread, mass accretion, binarity, and cirumstellar disk evolution. The scanning pattern allowed us to cover a contiguous field of approximately 600 arcmin^2 with both ACS and WFPC2, with a typical exposure time of approximately 11 minutes per ACS filter, corresponding to a point source depth AB(F435W) = 25.8 and AB(F775W) = 25.2 with 0.2 mag of photometric error. We describe the observations, data reduction, and data products, including images, source catalogs, and tools for quick look preview. In particular, we provide ACS photometry for 3399 stars, most of them detected at multiple epochs; WFPC2 photometry for 1643 stars, 1021 of them detected in the *U* band; and NICMOS *JH* photometry for 2116 stars. We summarize the early science results that have been presented in a number of papers. The final set of images and the photometric catalogs are publicly available through the archive as High Level Science Products at the STScI Multimission Archive hosted by the Space Telescope Science Institute.

Key words: brown dwarfs – ISM: individual objects (M42) – stars: formation – stars: low-mass – stars: pre-main sequence

Online-only material: color figures, machine-readable tables

1. INTRODUCTION

As the nearest active site of massive star formation, the Orion Nebula (Messier 42 and NGC 1976) and its associated young stellar cluster—the Orion Nebula Cluster (ONC)—provide a unique opportunity for studying the star formation process at the present epoch in our Galaxy (Pudritz 2002).

Young (a few Myr old), relatively massive ($\gtrsim 10^2$–10^3 $M_\odot$) stellar clusters like the ONC also contain, besides a large num-ber of low-mass objects ($M < 1$ $M_\odot$; Briceño et al. 2007), OB stars. These massive, early-type stars disrupt the placental molecular cloud and affect the evolution of the multitude of surrounding low-mass stars through their strong ionizing radiation, line-driven winds, and induced photoevaporative flows. Mass ejection from low-mass cluster members, close dynamical encounters, and substantial and variable X-ray emission also contribute to create a harsh environment which may critically affect planet formation (Bally et al. 2000; Scally et al. 2005; Eisner et al. 2008). Images of photoevaporating circumstellar disks taken with the *Hubble Space Telescope* (*HST*; e.g., O'Dell & Wong 1996) have shown that the canonical scenario for star formation, valid for isolated low-mass stars ($M \lesssim 1$ $M_\odot$) qui-etly forming in sparse, low-mass clusters (T associations), may not adequately account for typical star formation in rich clusters

---

(Lada & Lada 2003). As the Sun appears to have formed in a similar environment (Hester & Desch 2005; Williams & Gaidos 2007), understanding the ONC may shed light not only on key passages of the star and planet formation in general, but also on the origin of our own planetary system (Looney et al. 2006).

Due to its location and structure (O'Dell et al. 2008), the ONC can be studied in great detail. It is close ($d \simeq 436 \pm 20$ pc; O'Dell & Henney 2008), at relatively high galactic latitude ($b = -19°$, corresponding to 135 pc from the Galactic plane), and in an anticenter quadrant ($l = 209°$) with minimal foreground confusion. The large extinction of OMC-1 (up to $A_V = 50$ mag–100 mag) on the main ridge eliminates background confusion down to almost the H-burning limit (Hillenbrand & Carpenter 2000; Scandariato et al. 2011). The moderate extinction ($A_V = 1.5$ mag) caused by a foreground veil of neutral gas encompassing the nearest members of the ONC (O'Dell & Yusef-Zadeh 2000) allows detailed studies at visible wavelengths of individual stars.

The young stellar population of the ONC has been studied for decades. One of the most outstanding works to characterize the individual properties of these pre-main sequence (PMS) members is that of Hillenbrand (1997). In particular, she assembled a large photometric and spectroscopic database at visible wavelengths down to $I \sim 18$ mag. By estimating the stellar extinction for more than 1000 individual sources down to $\sim 1.0\ M_\odot$, she derived absolute luminosities, ages, and masses. More recently (Da Rio et al. 2009, 2010, 2012), the census of PMS stars in Orion has been extended and the stellar parameters derived for each source (e.g., effective temperature $T_{\rm eff}$ and luminosity $L_{\rm bol}$) further refined. The isochronal age of the ONC is about 1–2 Myr, with evidence for a spread in ages (Reggiani et al. 2011), although its actual extent in time is still debated (Jeffries et al. 2011). In what concerns the mass distribution, it peaks at about 0.3 $M_\odot$, but the shape of the stellar initial mass function (IMF) is highly dependent on the assumed evolutionary models (Da Rio et al. 2010).

Over the last decade several near-infrared surveys, both in imaging (e.g., Lucas & Roche 2000; Hillenbrand & Carpenter 2000; Luhman et al. 2000; Kaifu et al. 2000; Muench et al. 2002; Lada et al. 2000; Lucas et al. 2005) and in spectroscopy (e.g., Lucas et al. 2006; Slesnick et al. 2004; Riddick et al. 2007) have probed the IMF well into the brown dwarf regime down to the planetary mass range. The combination of photometry and spectroscopy is obviously a most powerful tool, allowing one to estimate the stellar parameters for individual sources; however, the spectroscopic surveys in the ONC have been limited either to the central part of the region, or to a sparse sampling of the entire cluster.

Despite the large amount of data collected over the years in the ONC, the accurate estimate of the properties of its population remains challenging. Fluxes of PMS stars are generally contaminated by UV and optical flux excesses due to accretion processes (Appenzeller & Mundt 1989; Gullbring et al. 1998) as well as by the near-infrared (Meyer et al. 1997) emission from circumstellar disks. Also, the differential extinction of the different sources partially embedded in the parental cloud limits a precise estimate of their properties, due to the strong degeneracy between $T_{\rm eff}$ and A_V (Hillenbrand 1997); this is mitigated by having at disposal multiple observed colors. Moreover, young stars show evident photometric variability (Herbst et al. 1994, 2002), which also introduces further uncertainties. For what concerns the substellar young members in Orion, their faint luminosity generally limits their optical observational

investigation to those least affected by dust extinction. Finally, the non-uniformity of the nebular background, both at large scales and in the local stellar vicinity (due to the possible presence of circumstellar material, either dusty disks or photoevaporating ones) requires imaging with high angular resolution, which is not achievable using ground-based facilities.

It is clear that under these circumstances, a panchromatic survey of the ONC with the high sensitivity and angular resolution of *HST* guarantees an unprecedented, outstanding data set which enables us to overcome these problems and attack the open questions about this star-forming region. Specifically, the main aspects to understand in depth are as follows. (1) What is the shape of the IMF, down to the lowest substellar masses in Orion? Does it differ from other star-forming regions, and from the Galaxy field? (2) What is the age of the system, and what have the time scales of its formation been? (3) How does mass accretion take place? How does it depend on the properties of the central objects? (4) What are the properties of the circumstellar disks, and to what extent are they affected by the harsh environment of the Orion Nebula? Can they form planets? (5) What are the properties of multiple stellar systems in Orion, and their circumstellar disks?

The particular abilities of *HST* to investigate the ONC were soon recognized in the early years of the mission, when Prosser et al. (1994) performed a photometric survey of the Trapezium region (Herbig & Tendrup 1986), the inner 0.3 pc (3.5 arcmin) of the ONC. Unfortunately, the photometry derived from these data, taken in 1991 with the spherically aberrated WFPC1, is subject to uncertainties as large as 0.4 mag. Several observing programs have been executed since then with all instruments on board *HST*, mostly dedicated to high-resolution imaging in narrowband filters of the central region to study the photoionized and dark silhouette disks (e.g., O'Dell & Wen 1994; McCaughrean & O'Dell 1996; Bally et al. 2000). A wide area survey (*HST* program GO-9825, PI: J. Bally) has also covered a large part of the Orion Nebula in the Hα filter of ACS.

The *HST* Treasury Program on the ONC, described in this paper, has been intended to perform the definitive study of the stellar component of the ONC at visible wavelengths. The program, awarded with a total of 104 orbits (Cycle 13, GO program 10246, PI: M. Robberto), has covered the brightest regions of the Great Orion Nebula at optical wavelengths, using broadband filters to obtain the most accurate photometry of the largest possible number of PMS objects. All imagers on board the *HST* have been used, namely, the Advanced Camera for Surveys in its Wide Field Channel mode (ACS/WFC), the Wide Field and Planetary Camera 2 (WFPC2), and the Near-Infrared Camera and Multi-Object Spectrograph (NICMOS) in Camera 3 mode. The *HST* observations have been complemented by a ground-based campaign that obtained nearly *simultaneous* photometry of the cluster from the U band to the K band (Da Rio et al. 2009; Robberto et al. 2010). Given the complexity of the observations, the nonconventional use of the *HST* and the large amount of data (more than 2000 single exposures) that were obtained, we provide in this paper a description of the program and a guide to the main data products. In Section 2, we describe the observations; in Section 3, we show the reduction and processing of the imaging data; and in Section 4, we present the details of photometry performed for each instrument. In Section 5, we summarize the data products we are publicly releasing, consisting of photometric catalogs and atlases, and mosaicked images. Finally, in Section 6, we outline the main

results that have been presented so far based on the *HST* Orion Treasury Program. Also, in the Appendix, we present in detail the realization of the spectacular color rendering of the region based on our ACS observations.

2. OBSERVATIONS

2.1. Instrument Characteristics and Setup

2.1.1. ACS

The ACS/WFC camera is based on a mosaic of two 2048×4096 pixel CCD detectors. The instrument optics deliver a spatial scale of ~ 50 mas pixel^{-1}, corresponding to a nominal field of view of $202'' \times 200''$. The two detectors are butted together on the long side with an interchip gap of approximately 50 pixels ($2''.5$). The readout noise is $\simeq 5\ e^-$ pixel^{-1} and the average dark current rate is $0.0038\ e^-$ s^{-1} pixel^{-1} (Maybathe et al. 2010).

We used the non-standard electronic gain of $2\ e^-$ ADU^{-1} in order to keep the detector saturation level, around $84{,}700\ e^-$, within the range of the 16 bit analog-to-digital converters. It has been shown (Gilliland 2004) that the CCDs of ACS remain almost perfectly linear ($<0.1\%$ discrepancy between relative count levels) up to saturation, and saturated charges spreading in the bleeding trails are fully preserved, allowing to recover the photometry of saturated sources with very high precision.

The off-axis optics of ACS introduce a skew image distortion between 7% and 10% of the field size. Since the pixels are projected as skew trapezoids on the sky, the fraction of sky area they actually map changes across the detector. This introduces a photometric error which can be corrected, as explained in Section 4.1.

2.1.2. WFPC2

The WFPC2 camera, now replaced by the Wide Field Camera 3, used four 800×800 pixel CCDs. Three of them image a $150'' \times 150''$ chevron-shaped region (WF, Wide Field) with a spatial sampling of 100 mas pixel^{-1}, the fourth one (PC, Planetary Camera) images a smaller $34'' \times 34''$ square field with 46 mas pixel^{-1} nested at the center of the chevron, in the fourth quadrant. Following the WFPC2 Instrument Handbook (McMaster et al. 2008), the nominal readout noise is 7.02, 7.84, 6.99, and $8.32\ e^-$ for the channels WF1–WF4. The mean dark current rate ($0.0045\ e^-$ s^{-1} pixel^{-1}) is comparable to the one of ACS.

Our observations were made when the WFPC2 instrument had already accumulated about 11 years of total radiation dose in a space environment, and was therefore affected by significant charge transfer efficiency (CTE) losses. The brightness of the Orion Nebula background, especially in broadband filters and at the center of the region, mitigates this problem. We applied the prescribed photometric correction (Dolphin 2000)[18] to our results (see Section 6), but still CTE losses represent the major source of noise and photometric uncertainty of the WFPC2 data. Concerning the gain setting, WFPC2 is equipped with 12 bit analog-to-digital converters. Their 4096 ADUs of dynamic range does not sample the full dynamic range of the CCD detector even with the highest selectable gain of $14\ e^-$ ADU^{-1}, which we have used. The photometric information of saturated (peak flux higher than about $53{,}000$ electrons) stars in WFPC2 images is therefore irremediably lost.

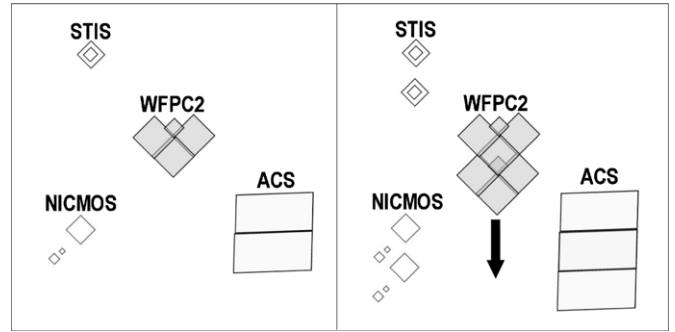[18] With updates at http://purcell.as.arizona.edu/wfpc2_calib/

Figure 1. Field of view of the *HST* instruments in the *HST* focal plane (prior to SM4) (left panel). The right panel shows the telescope shift between subsequent exposures chosen to optimize the coverage with both ACS and WFPC2.

2.1.3. NICMOS

The NICMOS instruments has three cameras, all equipped with a 256×256 HgCdTe detector but with different pixel scale. We selected Camera 3 (NIC3) because of its largest field of view, $51''.2 \times 51''.2$ with 200 mas pixel^{-1}, aiming to maximize the survey efficiency. NIC3 operates slightly out of focus with a loss in encircled energy beyond one pixel radius less than 10%–15%. This small degradation of the image quality partially compensates for the original undersampling of the NIC3 PSF. The equivalent readout noise of NICMOS depends on the adopted sampling scheme and on the number of reads. We used the sampling sequence STEP64 with NSAMP = 12 for the F110W filter and NSAMP = 11 for the F160W filter, providing 255 s and 192 s integration time, respectively. With these parameters, the readout noise is close to the nominal value of the instrument, around 27 electrons. We used the standard gain of $6.5\ e^-$ ADU^{-1}.

2.2. Observing Strategy

Our main scientific goals required a mosaic of the largest possible field in Orion with both ACS and WFPC2 in a number of broadband filters. The strategy we implemented exploited the relative position and orientation of the ACS/WFC and WFPC2 fields of view. We noted that the combination of size, offset, and position angle of the fields imaged by two instruments implies that the pointing move needed to image the same field seen by one of the two ACS CCDs with the other CCD causes the chevron pattern of WFPC2 to translate along its symmetry axis almost exactly by 1 ACS/WF chip (see Figure 1). Therefore, an ACS strip obtained by repeatedly offsetting the telescope by half of the ACS field of view produces a parallel, seamless herringbone pattern with WFPC2. A second scan, adjacent to the first one, can then be performed, maintaining full-field coverage with WFPC2 at the price a relatively modest (approximately 25%) overlap of the larger ACS/WFPC2 fields. By performing a third strip with the telescope rotated by $180°$, the relative positions of ACS/WFC and WFPC2 are exchanged. This third passage nicely complements the first two, providing contiguous area coverage of nearly the same field with both instruments.

We have repeated the 2+1 strip pattern three times, adjusting the length of each strip to cover the largest area of bright nebular background, where *HST* provides the greatest gain with respect to ground-based observations. The nine strips, numbered from 0 to 8, are oriented nearly in the east–west direction with position angles $100°$ or $280°$.

The full fields covered by the ACS/WFC and WFPC2 surveys are shown, respectively, in Figures 2 and 3. Both
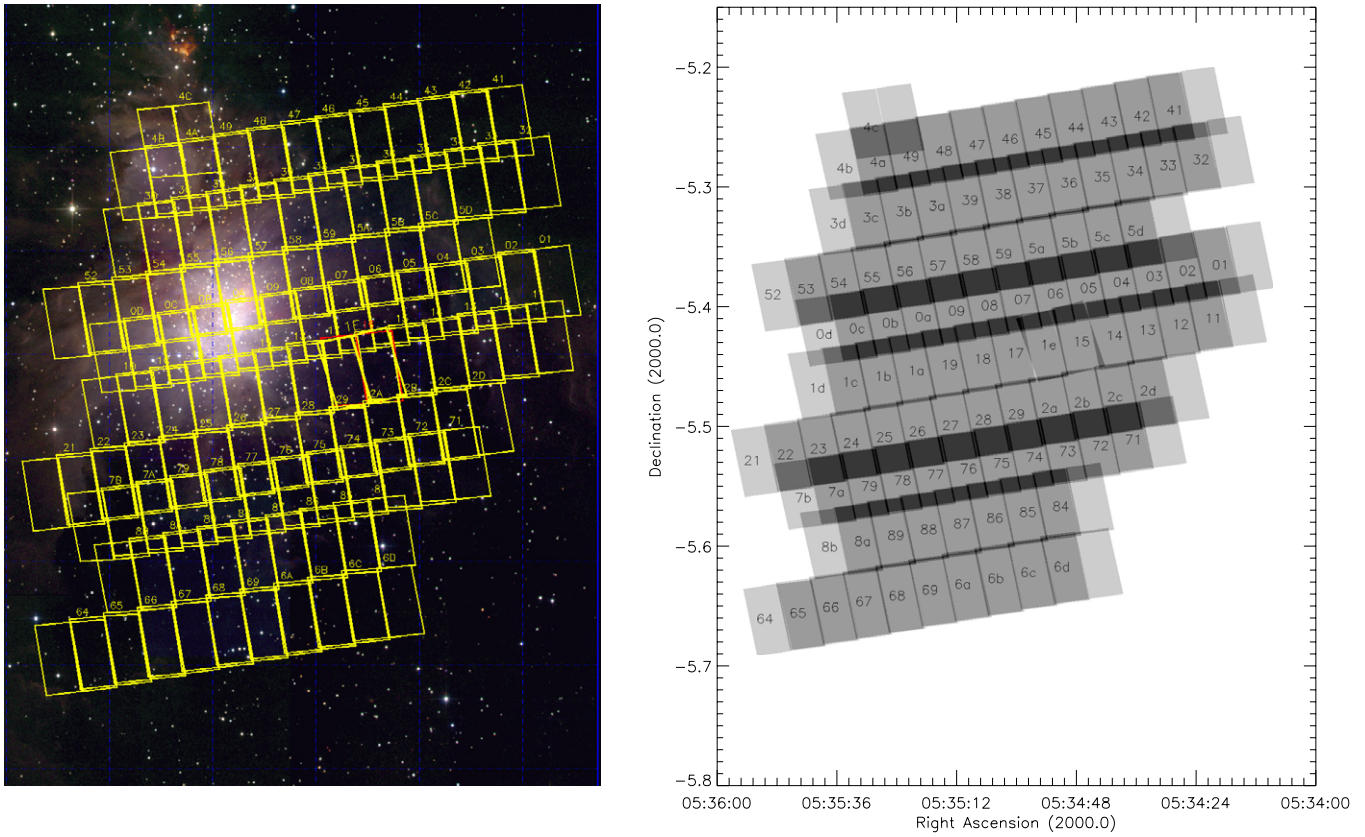
Figure 2. Total coverage of the ACS survey, superimposed to a color-composite *JHK* image of the Orion Nebula from 2MASS (left panel). The right panel highlights the overlapping regions between neighboring visits (darker gray shades), and reports the reference identification number of each of the individual visits.

(A color version of this figure is available in the online journal.)
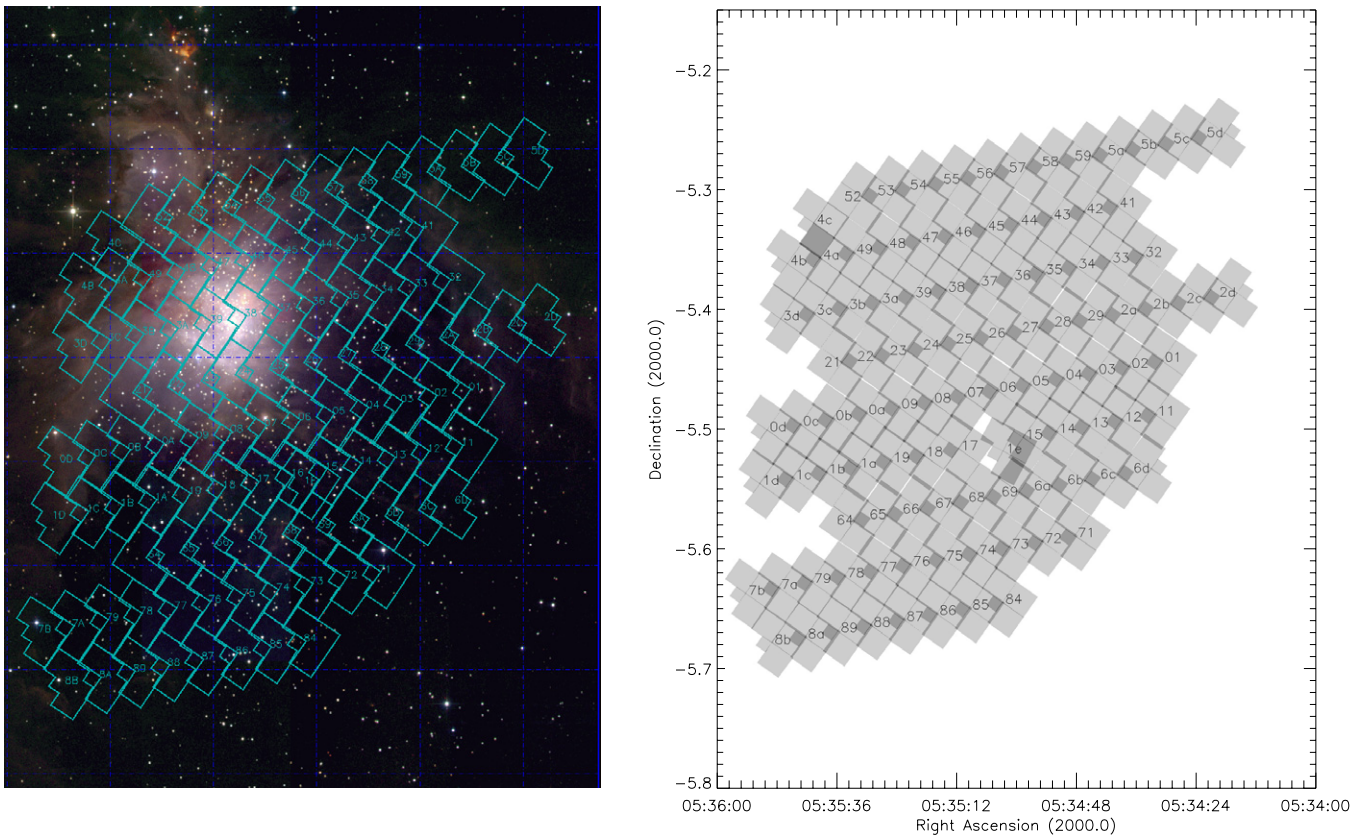

Figure 3. Same as Figure 2, for the WFPC2 survey.

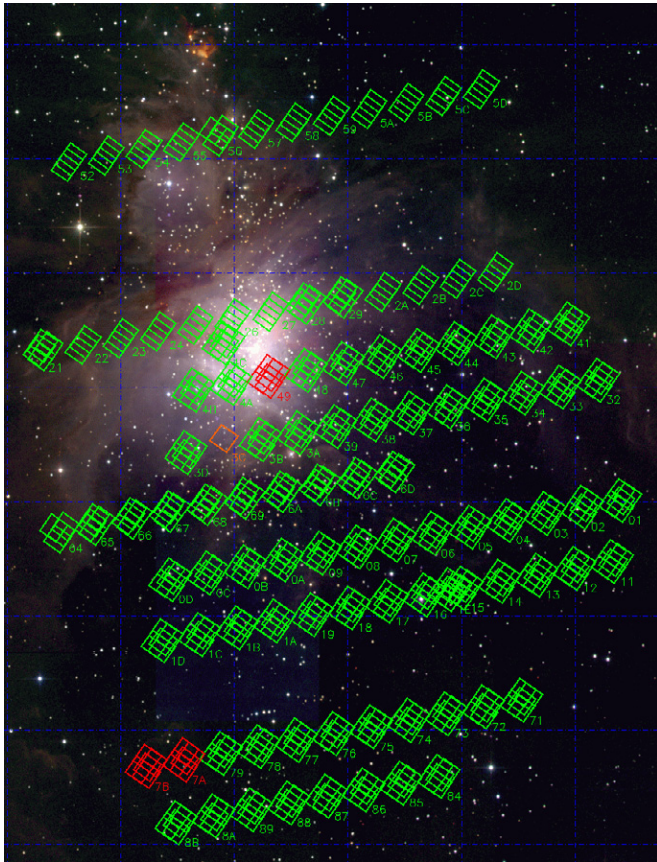(A color version of this figure is available in the online journal.)

Figure 4. Same as Figure 2 (left panel) for the NICMOS survey. Note that because of the small field of view of this instrument, the individual visits observed disjoint patches of the region. Fields marked in red denote visits affected by partial or total data loss (see Section 2.7).

(A color version of this figure is available in the online journal.)

Table 1
FOM Position Range

Detector	FOMXPOS (arcsec)	FOMYPOS (arcsec)
NIC1	−20.0 to +22.0	−21.0 to +23.0
NIC2	−20.0 to +22.0	−21.0 to +23.0
NIC3	−21.0 to +23.0	−37.0 to +8.0

equipped with a field offset mirror (FOM) which allows us to select the portion of the telescope focal plane falling on the detector. Moving the FOM, it is possible to probe a field larger than the nominal $52{\farcs}6 \times 52{\farcs}6$ of NIC3. The default FOM position had been optimized in the early days of instrument commissioning and before our program FOM moves had never been supported for science programs, for a number of good reasons: the image quality degrades at large distances from the optimal position, some vignetting is introduced at one FOM extreme of the offset range, and the moving mechanisms do not allow repositioning the FOM to better than one or two NIC3 pixels. Still, we were able to move the FOM, building for each visit a four-piece mosaic in the F160W band and a five-piece mosaic in the F110W band. Our request was granted on a shared risk basis, as the necessary changes to the NICMOS control software would have been tested "on-the-fly" using our observing time. Our first NICMOS observations, in fact, suffered from a number of FOM software limit errors. When this occurred, the FOM returned to its nominal central position and the following NICMOS observations within the same visit were suspended. This problem reoccurred for each visit scheduled using the same pattern. After each failure, the NICMOS operation team immediately investigated the cause of the error, implementing the needed changes. Soon we were able to move the FOM anywhere within the limits presented in Table 1, where we also include for reference the values for NIC1 and NIC2.

The improvements made with the scheduling of the NICMOS observations are illustrated in Figure 5 by the uneven shape of the fields covered with NIC3 across the field, the size of each tile being generally proportional to the "maturity" of the FOM control software. A total of 102 regions were covered in both the filter F110W and F160W bands, corresponding to about 177 arcmin^2 (15.9 Mpix) and 171.5 arcmin^2 (15.4 Mpix) in the F110W and F160W filters, respectively.

2.3. Scheduling

In order to exchange the relative position of ACS and WFPC2, we rotated by 180° the roll angle of the *HST* by scheduling the observations in two epochs separated by approximately 6 months. The first epoch, executed in the fall of 2004 (2004 October 11–November 7), covered strips 2, 5, and 6 with a position angle of 280°, for a total of 36 orbits. The second epoch, executed in the spring of 2005 (2005 March 3–April 26) covered strips 0, 1, 3, 4, 7, and 8 with a position angle of 100°, for a total of 68 orbits. Both epochs and position angles were optimized to schedule the observations at the peaks of the visibility periods of the Orion Nebula.

Table 2 summarizes the scheduling of our observations with the central coordinates of the field, for each instrument. In Figure 6, we present the overall coverage of the survey, limited on the central part of the ONC, with the field of view of all the instruments and for all the visits overlaid.

are approximately centered at R.A. = 05:35:00 and decl. = −5:26:00 (J2000.0), approximately 200″ to the SW of the Trapezium asterism and extend over about one-sixth of a square degree. In particular, the full ACS mosaic covers 627 arcmin^2 (corresponding to about 904 Mpix), whereas the WFPC2 mosaic covers 570.5 arcmin^2 (corresponding to 205.4 Mpix, assuming the 100 mas pixel^{-1} scale of the WFPC2 WFCs).

This scanning pattern typically provides, for each filter, two images with ACS with a few exceptions: (1) the half fields at the extremes of each strip, covered by only one CCD, are observed once; (2) the overlaid regions between adjacent strips are typically observed four times; (3) a small fraction of the ACS field is observed one or three times, in correspondence of the detector gaps, or in the case of a visit repeated with a different orientation (see Section 2.7). Further, smaller deviations are also occasionally present. For WFPC2, we typically have one passage per filter, except for the F336W band where the observations were split into two equal-length exposures (see Section 2.5). The areas observed with the WFPC2/PC have been generally observed also with the median detector (nr. 2) of the WFPC2/WF channel, with the exception of the very last field of each strip.

With NICMOS, our survey covered only a fraction of the ACS field due to the limited field of view of the instrument (Figure 4). However, we created a strategy to perform some field dithering and increase the area covered without moving the telescope during the visits. The NICMOS instrument is

Table 2
Observations Log

Target Name	Orient	Visit	ACS		WFPC2		NIC3	
			R.A. (2000.0)	Decl. (2000.0)	R.A. (2000.0)	Decl. (2000.0)	R.A. (2000.0)	Decl. (2000.0)
2005 Mar 31	100	01	05:34:16.80	−05:21:35.62	05:34:30.39	−05:26:36.2	5:34:12.23	−5:29:55.9
2005 Apr 1	100	02	05:34:23.40	−05:21:53.01	05:34:36.99	−05:26:53.6	5:34:18.83	−5:30:13.3
2005 Mar 30	100	03	05:34:29.99	−05:22:10.40	05:34:43.58	−05:27:10.9	5:34:25.42	−5:30:30.7
2005 Apr 3	100	04	05:34:36.76	−05:22:27.78	05:34:50.18	−05:27:28.3	5:34:32.02	−5:30:48.1
2005 Apr 2	100	05	05:34:43.18	−05:22:45.15	05:34:56.77	−05:27:45.7	5:34:38.61	−5:31:05.5
2005 Mar 30	100	06	05:34:49.78	−05:23:02.52	05:35:03.37	−05:28:03.1	5:34:45.21	−5:31:22.8
2005 Apr 5	100	07	05:34:56.37	−05:23:19.89	05:35:09.96	−05:28:20.4	5:34:51.80	−5:31:40.2
2005 Apr 5	100	08	05:35:02.96	−05:23:37.25	05:35:16.55	−05:28:37.8	5:34:58.39	−5:31:57.6
2005 Apr 6	100	09	05:35:09.56	−05:23:54.61	05:35:23.15	−05:28:55.2	5:35:04.99	−5:32:14.9
2005 Apr 6	100	0A	05:35:16.15	−05:24:11.96	05:35:29.74	−05:29:12.5	5:35:11.58	−5:32:32.3
2005 Apr 7	100	0B	05:35:22.75	−05:24:29.31	05:35:36.34	−05:29:29.9	5:35:18.18	−5:32:49.6
2005 Apr 8	100	0C	05:35:29.34	−05:24:46.66	05:35:42.93	−05:29:47.2	5:35:24.77	−5:33:07.0
2005 Apr 7	100	0D	05:35:35.94	−05:25:04.00	05:35:49.53	−05:30:04.5	5:35:31.37	−5:33:24.3
2005 Apr 7	100	11	05:34:18.22	−05:24:16.36	05:34:31.81	−05:29:16.9	5:34:13.65	−5:32:36.7
2005 Apr 7	100	12	05:34:24.82	−05:24:33.75	05:34:38.41	−05:29:34.3	5:34:20.25	−5:32:54.1
2005 Apr 4	100	13	05:34:31.41	−05:24:51.13	05:34:45.00	−05:29:51.7	5:34:26.84	−5:33:11.4
2005 Apr 8	100	14	05:34:38.00	−05:25:08.51	05:34:51.59	−05:30:09.1	5:34:33.43	−5:33:28.8
2005 Apr 8	100	15	05:34:44.60	−05:25:25.89	05:34:58.19	−05:30:26.4	5:34:40.03	−5:33:46.2
2005 Apr 9	100	17	05:34:57.79	−05:26:00.63	05:35:11.38	−05:31:01.2	5:34:53.22	−5:34:20.9
2005 Apr 9	100	18	05:35:04.39	−05:26:17.99	05:35:17.98	−05:31:18.5	5:34:59.82	−5:34:38.3
2005 Apr 9	100	19	05:35:10.98	−05:26:35.35	05:35:24.57	−05:31:35.9	5:35:06.41	−5:34:55.7
2005 Apr 9	100	1A	05:35:17.58	−05:26:52.70	05:35:31.17	−05:31:53.2	5:35:13.01	−5:35:13.0
2005 Apr 10	100	1B	05:35:24.17	−05:27:10.05	05:35:37.76	−05:32:10.6	5:35:19.60	−5:35:30.4
2005 Apr 10	100	1C	05:35:30.77	−05:27:27.40	05:35:44.36	−05:32:27.9	5:35:26.20	−5:35:47.7
2005 Apr 10	100	1D	05:35:37.36	−05:27:44.74	05:35:50.95	−05:32:45.3	5:35:32.79	−5:36:05.1
2005 Apr 26	287	1E	05:35:37.36	−05:27:44.74	05:35:02.22	−05:31:06.3	5:34:42.44	−5:33:27.7
2004 Nov 7	280	21	05:35:48.92	−05:31:39.11	05:35:35.33	−05:26:38.5	5:35:53.36	−5:23:20.1
2004 Oct 29	280	22	05:35:42.32	−05:31:21.77	05:35:28.73	−05:26:21.2	5:35:46.21	−5:23:09.2
2004 Oct 31	280	23	05:35:35.72	−05:31:04.42	05:35:22.13	−05:26:03.9	5:35:39.61	−5:22:51.8
2004 Oct 28	280	24	05:35:29.13	−05:30:47.07	05:35:15.54	−05:25:46.5	5:35:33.02	−5:22:34.5
2004 Oct 25	280	25	05:35:22.53	−05:30:29.72	05:35:08.94	−05:25:29.2	5:35:26.42	−5:22:17.1
2004 Oct 27	280	26	05:35:15.94	−05:30:12.36	05:35:02.35	−05:25:11.8	5:35:19.83	−5:21:59.7
2004 Oct 25	280	27	05:35:09.34	−05:29:55.00	05:34:55.75	−05:24:54.4	5:35:13.23	−5:21:42.4
2004 Nov 1	280	28	05:35:02.74	−05:29:37.63	05:34:49.15	−05:24:37.1	5:35:07.18	−5:21:18.6
2004 Nov 1	280	29	05:34:56.15	−05:29:20.26	05:34:42.56	−05:24:19.7	5:35:00.59	−5:21:01.2
2004 Oct 31	280	2A	05:34:49.55	−05:29:02.89	05:34:35.96	−05:24:02.3	5:34:53.44	−5:20:50.3
2004 Oct 31	280	2B	05:34:42.96	−05:28:45.50	05:34:29.37	−05:23:44.9	5:34:46.85	−5:20:32.9
2004 Oct 27	280	2C	05:34:36.36	−05:28:28.12	05:34:22.77	−05:23:27.6	5:34:40.25	−5:20:15.5
2004 Oct 29	280	2D	05:34:29.77	−05:28:10.73	05:34:16.18	−05:23:10.2	5:34:33.66	−5:19:58.1
2005 Apr 10	100	32	05:34:20.69	−05:16:19.80	05:34:34.27	−05:21:20.3	5:34:16.12	−5:24:40.1
2005 Apr 9	100	33	05:34:27.29	−05:16:37.19	05:34:40.88	−05:21:37.7	5:34:22.72	−5:24:57.5
2005 Apr 9	100	34	05:34:33.88	−05:16:54.57	05:34:47.47	−05:21:55.1	5:34:29.31	−5:25:14.9
2005 Apr 4	100	35	05:34:40.47	−05:17:11.94	05:34:54.06	−05:22:12.5	5:34:35.90	−5:25:32.3
2005 Apr 4	100	36	05:34:47.07	−05:17:29.31	05:35:00.66	−05:22:29.9	5:34:42.50	−5:25:49.6
2005 Apr 10	100	37	05:34:53.66	−05:17:46.68	05:35:07.25	−05:22:47.2	5:34:49.09	−5:26:07.0
2005 Apr 10	100	38	05:35:00.25	−05:18:04.04	05:35:13.84	−05:23:04.6	5:34:55.68	−5:26:24.4
2005 Apr 10	100	39	05:35:06.85	−05:18:21.40	05:35:20.44	−05:23:21.9	5:35:02.28	−5:26:41.7
2005 Apr 10	100	3A	05:35:13.44	−05:18:38.76	05:35:27.03	−05:23:39.3	5:35:08.87	−5:26:59.1
2005 Apr 9	100	3B	05:35:20.04	−05:18:56.10	05:35:33.63	−05:23:56.6	5:35:15.47	−5:27:16.4
2005 Apr 10	100	3C	05:35:26.63	−05:19:13.45	05:35:40.22	−05:24:14.0	5:35:21.74	−5:27:10.3
2005 Apr 9	100	3D	05:35:33.22	−05:19:30.79	05:35:46.81	−05:24:31.3	5:35:28.65	−5:27:51.1
2005 Apr 10	100	41	05:34:25.92	−05:13:51.70	05:34:39.50	−05:18:52.2	5:34:21.35	−5:22:12.0
2005 Apr 7	100	42	05:34:32.51	−05:14:09.09	05:34:46.09	−05:19:09.6	5:34:27.94	−5:22:29.4
2005 Apr 5	100	43	05:34:39.10	−05:14:26.47	05:34:52.68	−05:19:27.0	5:34:34.53	−5:22:46.8
2005 Apr 6	100	44	05:34:45.69	−05:14:43.84	05:34:59.27	−05:19:44.4	5:34:41.12	−5:23:04.2
2005 Apr 6	100	45	05:34:52.29	−05:15:01.21	05:35:05.87	−05:20:01.8	5:34:47.72	−5:23:21.5
2005 Apr 5	100	46	05:34:58.88	−05:15:18.58	05:35:12.46	−05:20:19.1	5:34:54.31	−5:23:38.9
2005 Apr 16	100	47	05:35:05.47	−05:15:35.94	05:35:19.05	−05:20:36.5	5:35:00.90	−5:23:56.3
2005 Apr 16	100	48	05:35:12.07	−05:15:53.30	05:35:25.65	−05:20:53.8	5:35:07.50	−5:24:13.6
2005 Apr 11	100	49	05:35:18.66	−05:16:10.65	05:35:32.24	−05:21:11.2		
2005 Apr 13	100	4A	05:35:25.25	−05:16:28.00	05:35:38.83	−05:21:28.5	5:35:20.68	−5:24:48.3
2005 Apr 13	100	4B	05:35:31.85	−05:16:45.35	05:35:45.44	−05:21:45.9	5:35:27.28	−5:25:05.7
2005 Apr 13	100	4C	05:35:26.57	−05:14:42.45	05:35:40.15	−05:19:43.0	5:35:22.00	−5:23:02.8
2004 Oct 28	280	52	05:35:44.81	−05:23:22.03	05:35:31.23	−05:18:21.5	5:35:48.70	−5:15:09.4
2004 Oct 30	280	53	05:35:38.22	−05:23:04.68	05:35:24.64	−05:18:04.1	5:35:42.11	−5:14:52.1

Table 2
(Continued)

Target Name	Orient	Visit	ACS		WFPC2		NIC3	
			R.A. (2000.0)	Decl. (2000.0)	R.A. (2000.0)	Decl. (2000.0)	R.A. (2000.0)	Decl. (2000.0)
2004 Oct 30	280	54	05:35:31.62	−05:22:47.33	05:35:18.04	−05:17:46.8	5:35:35.51	−5:14:34.7
2004 Oct 25	280	55	05:35:25.03	−05:22:29.98	05:35:11.45	−05:17:29.4	5:35:28.92	−5:14:17.4
2004 Oct 12	280	56	05:35:18.43	−05:22:12.62	05:35:04.85	−05:17:12.1	5:35:22.42	−5:13:58.9
2004 Oct 30	280	57	05:35:11.84	−05:21:55.26	05:34:58.26	−05:16:54.7	5:35:15.73	−5:13:42.6
2004 Oct 26	280	58	05:35:05.25	−05:21:37.89	05:34:51.67	−05:16:37.3	5:35:09.14	−5:13:25.3
2004 Oct 27	280	59	05:34:58.65	−05:21:20.52	05:34:45.07	−05:16:20.0	5:35:02.54	−5:13:07.9
2004 Oct 26	280	5A	05:34:52.06	−05:21:03.15	05:34:38.48	−05:16:02.6	5:34:55.95	−5:12:50.5
2004 Oct 26	280	5B	05:34:45.46	−05:20:45.77	05:34:31.88	−05:15:45.2	5:34:49.35	−5:12:33.2
2004 Oct 29	280	5C	05:34:38.87	−05:20:28.38	05:34:25.29	−05:15:27.8	5:34:42.76	−5:12:15.8
2004 Oct 30	280	5D	05:34:32.28	−05:20:10.99	05:34:18.70	−05:15:10.4	5:34:36.17	−5:11:58.4
2004 Oct 11	280	64	05:35:46.44	−05:39:34.96	05:35:32.85	−05:34:34.4	5:35:50.43	−5:31:21.2
2004 Nov 7	280	65	05:35:39.84	−05:39:17.61	05:35:26.25	−05:34:17.0	5:35:44.28	−5:30:58.6
2004 Nov 7	280	66	05:35:33.25	−05:39:00.25	05:35:19.66	−05:33:59.7	5:35:37.69	−5:30:41.2
2004 Nov 1	280	67	05:35:26.65	−05:38:42.89	05:35:13.06	−05:33:42.3	5:35:31.09	−5:30:23.8
2004 Nov 7	280	68	05:35:20.05	−05:38:25.52	05:35:06.46	−05:33:25.0	5:35:24.49	−5:30:06.5
2004 Nov 7	280	69	05:35:13.44	−05:38:08.15	05:34:59.85	−05:33:07.6	5:35:17.88	−5:29:49.1
2004 Nov 7	280	6A	05:35:06.86	−05:37:50.77	05:34:53.27	−05:32:50.2	5:35:11.30	−5:29:31.7
2004 Nov 6	280	6B	05:35:00.26	−05:37:33.39	05:34:46.67	−05:32:32.8	5:35:04.70	−5:29:14.3
2004 Nov 1	280	6C	05:34:53.66	−05:37:16.01	05:34:40.07	−05:32:15.4	5:34:58.10	−5:28:57.0
2004 Nov 1	280	6D	05:34:47.07	−05:36:58.62	05:34:33.48	−05:31:58.1	5:34:51.51	−5:28:39.6
2005 Apr 14	100	71	05:34:34.20	−05:30:20.73	05:34:47.79	−05:35:21.3	5:34:29.63	−5:38:41.0
2005 Apr 14	100	72	05:34:40.79	−05:30:38.12	05:34:54.38	−05:35:38.7	5:34:36.22	−5:38:58.4
2005 Apr 15	100	73	05:34:47.39	−05:30:55.50	05:35:00.98	−05:35:56.0	5:34:42.82	−5:39:15.8
2005 Apr 13	100	74	05:34:53.98	−05:31:12.89	05:35:07.57	−05:36:13.4	5:34:49.41	−5:39:33.2
2005 Apr 11	100	75	05:35:00.58	−05:31:30.26	05:35:14.17	−05:36:30.8	5:34:56.01	−5:39:50.6
2005 Apr 12	100	76	05:35:07.17	−05:31:47.63	05:35:20.76	−05:36:48.2	5:35:02.60	−5:40:07.9
2005 Apr 12	100	77	05:35:13.77	−05:32:05.00	05:35:27.36	−05:37:05.5	5:35:09.20	−5:40:25.3
2005 Apr 12	100	78	05:35:20.37	−05:32:22.36	05:35:33.96	−05:37:22.9	5:35:15.80	−5:40:42.7
2005 Apr 12	100	79	05:35:26.96	−05:32:39.72	05:35:40.55	−05:37:40.3	5:35:22.39	−5:41:00.0
2005 Apr 11	100	7A	05:35:33.56	−05:32:57.07	05:35:47.15	−05:37:57.6		
2005 Apr 11	100	7B	05:35:40.15	−05:33:14.42	05:35:53.74	−05:38:15.0		
2005 Apr 11	100	84	05:34:48.72	−05:33:40.42	05:35:02.31	−05:38:41.0	5:34:44.15	−5:42:00.7
2005 Apr 11	100	85	05:34:55.32	−05:33:57.80	05:35:08.91	−05:38:58.3	5:34:50.75	−5:42:18.1
2005 Apr 11	100	86	05:35:01.91	−05:34:15.17	05:35:15.50	−05:39:15.7	5:34:57.34	−5:42:35.5
2005 Apr 14	100	87	05:35:08.51	−05:34:32.54	05:35:22.10	−05:39:33.1	5:35:03.94	−5:42:52.9
2005 Apr 14	100	88	05:35:15.11	−05:34:49.90	05:35:28.70	−05:39:50.4	5:35:10.54	−5:43:10.2
2005 Apr 15	100	89	05:35:21.70	−05:35:07.26	05:35:35.29	−05:40:07.8	5:35:17.13	−5:43:27.6
2005 Apr 15	100	8A	05:35:28.30	−05:35:24.61	05:35:41.89	−05:40:25.2	5:35:23.73	−5:43:44.9
2005 Apr 15	100	8B	05:35:34.90	−05:35:41.96	05:35:48.49	−05:40:42.5	5:35:30.33	−5:44:02.3

2.4. Visit Configuration

In order to use simultaneously all imaging instruments on board *HST*, we pushed to the limit the capability of the telescope to handle parallel, asynchronous observations. When different *HST* instruments are operated in parallel, they ultimately compete to access the main solid state recorder (SSR) of the spacecraft to dump their data. We looked for a timing pattern that provides the highest possible observing efficiency while maintaining in the background a nearly continuous data transfer activity.

We configured each pointing as a one-orbit visit. Figure 7 shows how the various exposures were distributed during each visit. After the initial guide star acquisition, the three instruments simultaneously started the observations. The exposure time with ACS has been finetuned to allow continuous operations with buffer dump activity during the successive exposure or, in the case of the last image, during the occultation, leaving just 1 s of unused visibility time. At the same time NICMOS obtained nine images and WFPC2 obtained five images; the first two images

on WFPC2 are the short ones, in order to access the SSR before the first data dump from ACS.

2.5. Filters and Exposure Times

As shown in Figure 7, a total of 19 images were taken on each visit. The filters, exposure times, and observing strategies are given in Table 3 and the filter transmission curves are presented in Figure 8.

The motivation for the choice of the filters is the following. The broadband ACS filters, F435W, F555W, F775W, and F850LP have been adopted for the main broadband photometric survey. We estimated that all ONC members down to below the substellar masses, with the exception of the brightest stars whose bleeding trail could fall out of the detector edges, would have provided enough signal in at least two ACS bands to allow constraining their stellar colors and therefore, given their spectral types, their reddening, and absolute luminosity. The ACS F658N Hα filter is intended for mapping circumstellar matter with the highest possible resolution, mostly to discriminate extended sources and assess the presence of circumstellar
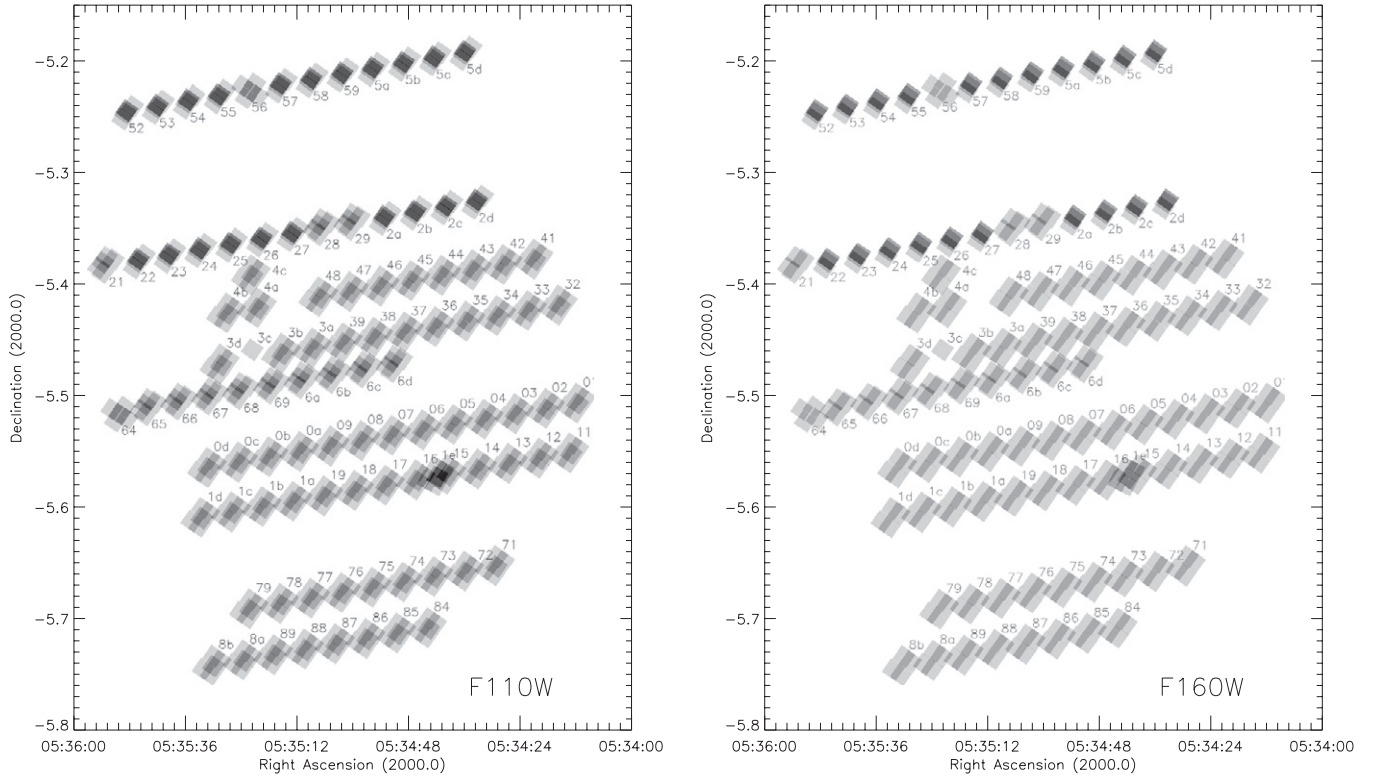
Figure 5. Same as Figure 2 (right panel) for the NICMOS F110W (left panel) and F160W (right panel).

Table 3
Visit Structure

Instrument	Filter	Ground Equivalent	Exposure	Integration Time (s)	Zero Point (VegaMag)
ACS/WFC	F435W	Johnson B	6	420	25.779
ACS/WFC	F555W	Johnson V	9	385	25.724
ACS/WFC	F658N	Broad Hα	1	340	22.365
ACS/WFC	F775W	Sloan i	8	385	25.256
ACS/WFC	F850LP	Sloan z	7	385	24.326
WFPC2	F336W	Johnson U	17, 18	400×2 (CR-SPLIT)	20.279
WFPC2	F439W	Johnson B	4	80	20.107
WFPC2	F656N	Narrow Hα	19	400	16.819
WFPC2	F814W	Cousin I_c	5	10	20.845
NIC3	F110W	J band	2, 11, 12, 15, 16	256×5 pointing FOM dither	22.50
NIC3	F160W	H band	3, 10, 13, 14	192×4 pointing FOM dither	21.66

Notes. Actual number of pointings for NIC3 may be lower (see Section 2.7). To convert from total counts (DN) to magnitude, use the relation magnitude $= -2.5 \log(\text{DN/Exptime}) + $ Zeropoint.

emission or dark silhouette disks. The WFPC2 F336W filter was intended to probe the accretion luminosity and therefore the mass accretion rates on the ONC stars, along the lines of the earlier work by Robberto et al. (2004). Since this filter is affected by red leak, we have added a short exposure in the F814W filter to simultaneously probe the spectral region of the red leak and get a measure of the contamination unaffected by stellar variability. The F439W filter of WFPC2 also allows for a solid measure of the Balmer jump. Finally, the WFPC2 F656N filter is a narrowband Hα filter which does not pass the [N II] line and has therefore stronger diagnostic power than the broader ACS F658N filter, contaminated by the [N II] line at $\lambda = 6583$ Å. For NICMOS, the F110W and F160W filters on NIC3 were adopted to provide the deepest images of the fields ever obtained in the near-IR.

Due to FOM dithering pattern, the integration times of the combined NICMOS exposures varies across the mosaics, ranging between 192 and 762 s in filter F160W and 256 and 1280 s in filter F110W, the central parts of each sub-mosaic being imaged for the full amount of time. About 55% of the mosaics are covered for 192 s in the F160W band, and 40% for 380 s. For the F110W filter, around 45% is covered for 256 s, and 40% for 512 s.

2.6. Cosmic-Ray Removal Strategy

Our observing strategy, optimized to map the largest possible field with all instruments on board *HST*, is less than ideal in what concerns the removal of cosmetic defects, cosmic rays in particular. We have therefore adopted the following strategy: for ACS, where we have typically two (and occasionally more)
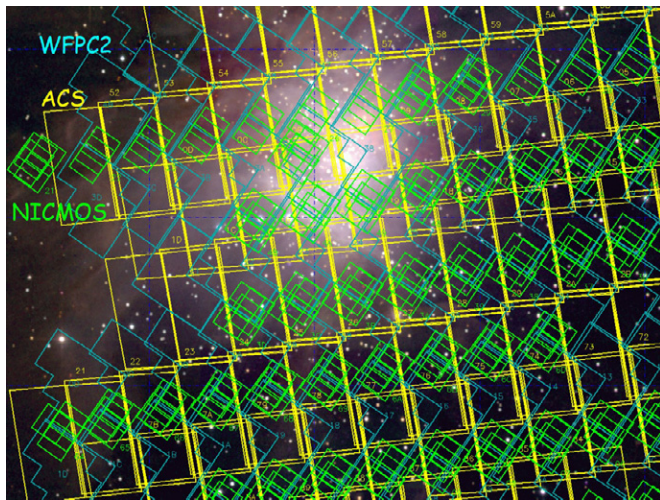
Figure 6. Coverage of the survey for all the three cameras, limited for the central part of the region. See also Figures 2, 3, and 5.

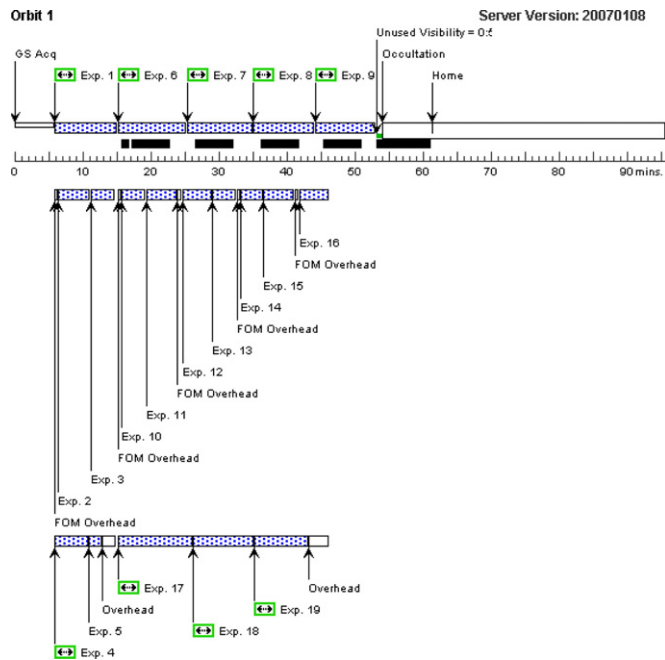(A color version of this figure is available in the online journal.)

Figure 7. Sequence of observations of a typical *HST* orbit of our program.

(A color version of this figure is available in the online journal.)

images, cosmic rays were removed by adopting the value found in the other image(s), when available (see Section 3.3).

The same strategy has been adopted for the F336W images of WFPC2, which come in pairs without dithering moves. For the other filters, taken as single images, we used the IDL routine `la_cosmic.pro`[19] written by Joshua Bloom (Caltech) based on the Laplacian algorithm originally developed by van Dokkum (2001).

Finally, NICMOS image have been taken in Multiaccum mode sampling the integration signal as it accumulates on the detector. This allowed us to eliminate cosmic-ray events using the standard NICMOS pipeline.

---

[19] Available at http://www.astro.yale.edu/dokkum/lacosmic/la_cosmic.pro
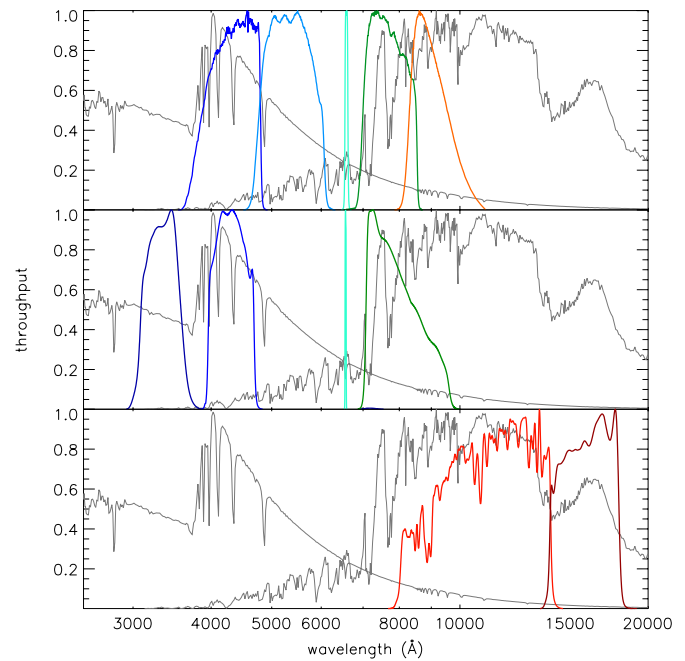
Figure 8. Passbands of the 11 filters used for our program. Top: ACS filters, from left to right: F435W, F555W, F658N, F775W, and F850LP; middle: WFPC2 filters, from top to right: F336W, F439W, F656N, and F814W; and bottom: NICMOS filters, from left to right: F110W and F160W. The gray lines represent the spectrum of an A0V star, according to the Nextgen model (Hauschildt et al. 1999) for a 10,000 K atmosphere, and an M6V star according to the AMES-MT model (Allard et al. 2000) at 3000 K.

(A color version of this figure is available in the online journal.)

2.7. Anomalies and Lost Data

The brightness and stellar density at the core of the Orion Nebula reduces the number and reliability of useful guide stars. Spurious sources (extended, binaries) cause loss of guide on the Fine Guide Sensors (FGSs) of the telescope. In most cases, the problems we encountered during the observations were minor. In a number of visits, only one guide star (instead of the two usually required) was available and the orientation of the telescope had to be maintained by the less accurate gyroscopes. This, together with the catalog errors in the absolute position of the guide stars, causes the images to be slightly misaligned with respect to their nominal position. On the other hand, due to the relatively short exposure times we generally adopted, it did not result in a significant degradation of the point-spread function (PSF). Only in a few occasions did we encounter major anomalies.

1. Visit 01: only one of the two F336W images was taken with WFPC2.
2. Visit 16: lost due to failed guide star acquisition. This visit was successfully repeated on 2005 April 26 as visit 1E, with slightly different orientation (see Figures 2 and 3).
3. Visit 17: the F435W exposure with ACS was interrupted at 75% of total exposure time due to the loss of guide star. The previous F658N exposure, also with ACS, was completely lost.
4. Visit 57: like visit 17, the F435W exposure with ACS was interrupted at 80% of total exposure time due to the loss of guide star.

NICMOS observations also experienced anomalies, related either to the guide star errors or to the errors in the commanding of the FOM.

1. Visit 49, 7A, 7B: lost due to the NICMOS suspend error triggered by FOM error.

2. Visits 3C: partial data loss due to NIC suspend error for FOM error. Only the first F110W and F160W pattern positions were acquired.

2.8. File Naming Convention

To facilitate data retrieval from the *HST* archive, we provide a legend for the image file names. The original fits file naming convention follows the general nine-letter *IPPPSSOOT* keyword of the *HST* data sets, where

1. *I* refers to the instrument, i.e., *I = j* for ACS, *I = u* for WFPC2, and *I = n* for NICMOS;
2. *PPP* refers to the program identification, which in the case of the *HST* Treasury Program is *PPP = 93k*;
3. *SS* refers to the visit number, varying between *SS = 01* and *SS = 8D*;
4. *OO* refers to the observation number during each visit; for ACS and NICMOS this is an hexadecimal code which changes with each individual observation (exposure), whereas for WFPC2 it cycles through the same values according to the following list: 01 = F439W; 02 = F814W; 03 = F336W; 04 = F336W; and 05 = F656N;
5. *T* refers to a data-transmission code from the *HST* spacecraft. In our case, it is always *T = M* (merged) for ACS and NICMOS, whereas it is *T = Q* (retransmitted) for WFPC2.

3. DATA REDUCTION AND PROCESSING

3.1. ACS *_flt.fits Images

Each of the 104×5 ACS exposures was run through the ACS on-the-fly reprocessing (OTFR) pipeline, which delivers 4096×4096 pixel images corrected for bias, dark current, and flat field. OTFR corrected images take the FLT suffix (*_flt.fits). The *_flt.fits images are still affected by the geometric distortion introduced by the ACS optics, mostly an 8% compression of the ratio of the diagonals. As a result, WFC pixels project on the sky as rhombuses rather than as squares. Varying nonlinearly with field position, geometric distortion introduces a photometric error by up to 9%, depending on the sky area imaged by each pixel.

Geometric distortion, and the associated photometric error, can be corrected using, e.g., the drizzle package, discussed in Section 3.3. However, when only a few dithered images are available (as in our case), it is more appropriate to extract the source photometry from the geometrically distorted *_flt.fits images, correcting only for the photometric error by multiplying the *_flt.fits images by the pixel area map correction (PAM; Gonzaga et al. 2011). In the case of ACS/WFC, the PAM represents the fraction of nominal sky area ($0\rlap{.}''05 \times 0\rlap{.}''05$) seen by each pixel. By avoiding resampling the images into a different projection, this approach preserves the original sharpness of both real stellar images and artifacts like bleeding trails and cosmic rays. Working on individual images rather than mosaicked images can also yield better photometry in some cases. For example, stars that are significantly variable can be mistakenly identified as being affected by cosmic rays in the mosaicing process, resulting in pixels near the PSF core being corrupted in the mosaic. Sticking with the individual images for the photometry avoids this problem. Our ACS photometry has therefore been obtained on PAM-corrected *_flt.fits images (see Section 4).

3.2. ACS F850LP Fringing

The two CCDs of ACS, thinned and backside illuminated, may be affected by fringing longward of 7500 Å due to the interference between the incident light and the light internally reflected at the interface between the thin layers of the chip. This problem affects our F850LP ACS images. On the ground, fringing is usually due to atmospheric airglow lines. In our case, it is due to the nebular emission of the Orion Nebula, dominated in the F850LP passband by the [S III] lines at 9069 Å and 9532 Å, in a ratio of approximately 1:3 (Osterbrock et al. 1992). The Pa7 line at 10049 Å is a lesser contributor whereas the He I 10830, intrinsically about as strong as the stronger 9069 Å [S III] line, is damped by the low quantum efficiency of CCDs at this wavelength and contributes negligibly in comparison to the other lines. The fringing pattern produced by an extended source like the Orion Nebula varies across the field following the relative brightness distribution of the emission lines. This complicates its suppression through image processing.

To mitigate fringing, we created a fringe flat field by filtering out both low and high spatial frequencies from our F850LP images. Then, we combined the fringe flat with that obtained from the ACS fringe optical model for the [S III] 9069 Å and 9532 Å lines of Walsh et al. (2003). This reduced the peak-to-peak amplitude of the fringe pattern from ∼10% to less than 2%, making our F850LP *_flt.fits images largely unaffected by fringing.

3.3. ACS Drizzling

To remove cosmic rays and combine the images into a single mosaic aligned with a global astrometric reference frame we use the Multidrizzle software (Fruchter & Hook 2002; Fruchter et al. 2009). Multidrizzle takes as input the *_flt.fits images and returns them as *_drz.fits *drizzled* images corrected for distortion, aligned on the common astrometric grid and cosmic ray cleaned. Then, it combines the *_drz.fits images into a single image, which usually represents the final *HST* data product with optimal depth, cosmetic quality, and improved sampling of the PSF.

For a survey area as large as the one imaged by our program, the alignment of the distortion corrected *_drz.fits images into a single astrometric frame is generally rather complex. The astrometric information originally stored in the original FITS image header, calculated on the basis of the nominal parameters of the instrument and telescope pointing, is not accurate enough. This because the absolute position of the *HST* guide stars is typically known with an uncertainty of about $0\rlap{.}''5$–$1''$, i.e., 10–20 ACS/WFC pixels. Guide star position errors affect not only the relative offset between the drizzled ACS images, but also induce a rotation error: as the observations are generally performed locking the FGSs on two different guide stars typically separated by about $25'$, there is an orientation error as large as $2'$ in position angle, of the order of one pixel at the edge of the ACS field. In general, therefore, the astrometric correction stored in the fits header as World Coordinate System (WCS) parameters must be corrected before drizzling.

In the case of our ACS mosaic, the large shifts between images and the relatively low number of point-like sources made the alignment procedure especially challenging. Our final strategy has been based on the following steps.

1. First, a copy of the F850LP and F775W *_flt.fits images was smoothed with a Gaussian filter and subtracted from the original ones to remove most of the non-uniform

background; SExtractor (Bertin & Arnouts 1996) was then run to derive the position of the sources; the coordinates of unsaturated source in at least one of the two filters were matched and merged to reduce the possibility of contamination by clusters of cosmic rays. This resulted in an initial input catalog of sources.

2. We concentrated on the F850LP images, as this filter yields the largest number of usable sources. The X, Y positions of all unsaturated point sources in the F850W *_flt.fits images were accurately measured using the IRAF two-dimensional (2D) Gaussian centering routine.

3. The measured X, Y positions were corrected for geometric distortion using the Anderson (2006) distortion model, known to be accurate to better than ~0.1 pixels, i.e., less than 5 mas, across the extent of the ACS/WFC *_flt.fits images.

4. For each of the nine ACS strips, the distortion-corrected X, Y positions of stars measured in adjacent visits were matched and placed on a common grid. Starting from the image at one extreme of the strip, the other images were registered using a linear plate model transformation of this type:

$$x_2 = \Delta x + ax_1 + by_1 \qquad (1)$$

$$y_2 = \Delta y + cx_1 + dy_1, \qquad (2)$$

where the parameters $\Delta x, \Delta y, a, b, c,$ and d, giving the location of the tile on the strip, were determined through a minimization procedure; the typical rms of the linear fit resulted about 1 mas.

5. A master catalog was built for each strip, listing all distortion-corrected, registered, and averaged X, Y positions.

6. The sources on each master catalog with counterparts in the Two Micron All Sky Survey (2MASS) catalog were identified and a least-squares solution was found to derive their R.A. and decl. in the 2MASS system.

The shifts calculated for each strip were used to update the WCS information in the corresponding *_flt.fits header file. These new updated flat-fielded images were used as input to MultiDrizzle. The same shifts derived for the F850LP filters were used for the other filters, since all exposures within a visit were taken without moving the telescope and the positional offsets between different filters are generally smaller than a pixel.

The *_drz.fits images are corrected for cosmic rays. Cosmic-ray removal was done in the driz_cr step of Multidrizzle by comparing the value of a pixel in each input image to the "min" or "median" combination of the values in the other images. This process is extremely sensitive to alignment errors and source variability. If the alignment is less than perfect, the very sharp PSF core of the (normally two in our case) detections may fall on different pixels and therefore be flagged as cosmic rays and removed in the following combination step. An early attempt of combining frames from multiple strips into a few large "supertiles" of $14,000 \times 13,000$ pixels resulted in images with less than optimal astrometric and photometric quality. It was found that the best results in the image registration could be obtained working on a strip-by-strip basis, i.e., with images taken with the same telescope orientation. To keep the size of the reduced images below 1 GB, we had to split each final strip in two halves, left and right. The full set of drizzled images,

Table 4
Visits Included in ACS Drizzled Strips

Strip	Visits
0R	01, 02, 03, 04, 05, 06, 07
0L	07, 08, 09, 0a, 0b, 0c, 0d
1R	11, 12, 13, 14, 15, 1e, 17
1L	17, 18, 19, 1a, 1b, 1c, 1d
2R	27, 28, 29, 2a, 2b, 2c, 2d
2L	21, 22, 23, 24, 25, 26, 27
3R	32, 33, 34, 35, 36, 27, 38
3L	37, 38, 39, 3a, 3b, 3c, 3d
4R	41, 42, 43, 44, 45, 46, 37
4L	45, 46, 47, 48, 49, 4a, 4b, 4c
5R	57, 58, 59, 5a, 5b, 5c, 5d
5L	52, 53, 54, 55, 56, 57, 58
6L	67, 68, 69, 6a, 6b, 6c, 6d
6R	64, 65, 66, 67, 68, 69, 6a
7L	71, 72, 73, 74, 75, 76, 77
7R	75, 76, 77, 78, 79, 7a, 7b
8L	84, 85, 86, 87, 88, 89, 8a
8R	85, 86, 87, 88, 89, 8a, 8b

produced with the standard north-up, east-left orientation, is thus composed of 18 mosaics per filter, each one corresponding to half of a strip. The visits included in each strip are listed in Table 4. The early set of $14,000 \times 13,000$ supertiles was used to produce the large color picture of the Orion nebula, as described in the Appendix.

The celestial coordinates reported in our source catalog are in the absolute astrometric reference of 2MASS, with a precision of the order of a few tens of milliarcsecond, as the typical 2MASS precision for a single source is ~100 mas (Skrutskie et al. 2006). Their relative positions, however, preserve the centroid precision of ACS/WFC of a few milliarcseconds (depending on the brightness of the sources, of the background, and on the source morphology). Accurate astrometric analysis should therefore be performed only on sources belonging to the same strip.

3.4. WFPC2

WFPC2 images were processed through the standard calwp2 calibration software implemented in the OTFR pipeline. The pipeline removes additive (bias, dark current) and multiplicative (flat field) effects, besides flagging static bad pixels and correcting for instrumental artifacts. As anticipated in Section 2.6, cosmic-ray corrections on the F336W images, taken as CR-SPLIT pairs, was performed using the same minimization routine used for the ACS data, whereas for the other filters we used a Laplacian filter (van Dokkum 2001).

We applied delta flats for the WF4 chip of the F336W images to correct for artifacts created by dust spots on the optics that had moved after the standard flat-field frames had been taken. The delta-flat frames were created by stacking all of the WF4 frames, excluding those containing bright stars or with bright areas of nebulosity. In total, 44 images were used for the first epoch and 50 for the second. The frames were first divided by their mean value and then were median averaged with $\pm 2.5\sigma$ clipping. Photometry checks showed that the results obtained on the images with and without the delta-flat corrections coincide within 2%. We also removed bias jumps, mostly occurring in the second epoch (spring) data, following the guidelines reported on the WFPC2 Web site.[20]

---

[20] http://www.stsci.edu/hst/wfpc2/wf4_anomaly.html

3.5. NICMOS

NICMOS images were reduced using the 4.1.1 version of the CALNICA calibration pipeline, with the exception of custom dark reference files. The CALNICA procedure subtracts the analog to digital converter bias level, accounts for signal accumulated at the time of the first read, corrects for detector nonlinearities, estimates signal rates and rejects cosmic rays fitting the sequence of non-destructive reads, performs dark and flat-field correction, and removes static image artifacts.

The second part of the image processing was performed using the CALNICB pipeline, which allows the removal of the background illumination pattern. As an additional processing step, we corrected for vignetting by using the ratio of one of our vignetted exposures in the central region of the cluster with the 3×3 NICMOS mosaic of the Trapezium obtained in 1998 (Luhman et al. 2000) to derive a first-order correction. A smooth function was fit to the vignetted edge in the ratio image and then expanded into a 2D vignetting correction image (one per filter for F110W and F160W) that was applied to all affected exposures. A further "delta-flat" correction was applied by median averaging all images taken at the same FOM positions, rejecting those more affected by diffuse nebular emission or point sources. After determining the offsets of individual images of each region by measuring the centroids of common stars, all images belonging to the same dither group were distortion corrected and combined using WDRIZZLE Version 3.4.1 into a 800×800 image, preserving the nominal scale of 0.2 arcsec pixel^{-1} and with an alignment such that pixel (129, 129) of the central image of each group falls at pixel (401, 401) of the output image. A final cosmic ray and bad pixel rejection process was performed using a custom rejection procedure that compares minimum and median values of pixels common to multiple frames. Absolute astrometry was obtained, for all fields but one, using both 2MASS (primary) and ISPI (secondary) catalogs (see Section 4.3).

4. PHOTOMETRY

4.1. ACS Photometry

In Section 3.3, we have described the construction of the ACS source catalog, containing a total of 8185 entries, including multiple detections. As anticipated in Section 3.1, photometry extracted from our ACS drizzled images is prone to errors because of both source variability and the limited number of dither pointing used to produce the image. Having typically only two exposures, often taken days apart, the cosmic-ray removal algorithm may flag as cosmic ray the PSF core of the brighter image. To ensure photometric accuracy, our main photometric catalog has therefore been extracted from the *_flt.fits images. This means that our source catalog will report, in most cases, multiple detections for each source, one for each visit.

As the *_flt.fits images are affected by cosmic rays, for each source and each filter we carefully tuned the aperture radius to avoid the presence of a cosmic ray. Aperture photometry was then obtained using a typical extraction radius of 10 pixels, occasionally reduced to exclude a cosmic ray. Typical sky annuli were between 10 and 15 pixels, but when visual inspection showed strong spatial variability of the background, the sky annulus was adjusted accordingly to get a more reliable estimate of the local background.

Having used a gain of 2 e^- ADU^{-1} (see Section 2.1.1), we could also extract the photometry of isolated saturated sources

up to blooming distances of about 10 pixels. Our final catalog lists, for each source, the number of saturated pixels in the bleeding trails within the aperture and the maximum distance from the center. Sources with a larger bleeding trail usually require careful processing to optimize the extraction area and prevent the inclusion of nearby sources. While we do not provide their photometry, further analysis may allow us to recover a few more bright sources.

Working with a range of extraction radii, we had to apply an aperture correction to our measures. We considered the possible errors introduced by directly applying the standard ACS aperture corrections of Sirianni et al. (2005), as they were derived on drizzled, distortion-corrected images instead of our *_flt.fits images. To address this point, we compared the stellar fluxes measured in our *_flt.fits images with those derived from the corresponding *_drz.fits images. In general, one expects *_drz.fits images to show broader PSFs cores than the *_flt.fits images, especially when only a few images are available. We found that for aperture radii larger than about 10 pixels the stellar fluxes extracted in the *_drz.fits and *_flt.fits images are the same, allowing us to use the aperture corrections and uncertainties tabulated by Sirianni et al. (2005). For aperture radii smaller than 10 pixels, the comparison showed some scatter. This is not surprising, considering that our sample is not ideal to measure small systematic effects, due to the paucity of objects, the non-uniform background, and the possible contamination from circumstellar matter in young stellar objects. In order to measure the ratio between fluxes at radii $r < 10$ pixels and $r = 10$ pixels we selected "midrange" sources, neither saturated or too faint in the *_flt.fits images, and averaged the results through a σ-clipping routine to reject outliers. The corrections derived are consistent (within 1σ) with the standard ACS photometric aperture corrections of Sirianni et al. (2005). On these grounds, we assumed as a baseline the Sirianni et al. (2005) aperture corrections at all radii.

We also corrected our photometry for the ACS/WFC CCDs CTE using the correction formula of the Instrument Science Report ACS 2004-006 (Riess & Mack 2004). The CTE correction turned out to be very small, primarily because of the generally high background due to the strong nebular emission. Our final step was to apply the photometric zero points. We adopted the standard VEGAMAG photometric system tabulated by Sirianni et al. (2005).

In Figure 9, we present the calibrated magnitudes versus their corresponding errors for the five ACS filters. Our 5σ sensitivity limit ($\sigma_{\mathrm{mag}} \simeq 0.2$) are about $m[\mathrm{F435W}] = 26$, $m[\mathrm{F555W}] = 25.5$, $m[\mathrm{F658N}] = 22.5$, $m[\mathrm{F775W}] = 25.3$, and $m[\mathrm{F850LP}] = 24.2$ in the Vega system.

In Figure 10, we show the spatial distribution of the ACS sources in the final catalog, color coded according to their color. In Figure 11, we present the same for the highly crowded central region of the ONC.

4.2. WFPC2 Photometry

WFPC2 sources were identified by looking for counterparts to our ACS (Ricci et al. 2008) and ISPI (Robberto et al. 2010) photometry. We preferred this approach, instead of considering all possible detections on the WFPC2 frames, in order to suppress the possible contamination from spurious effects in the aging CCD detectors. Both the ACS and ISPI catalogs have a significantly deeper detection limit, both due to the higher exposure times and because of the longer wavelengths—therefore
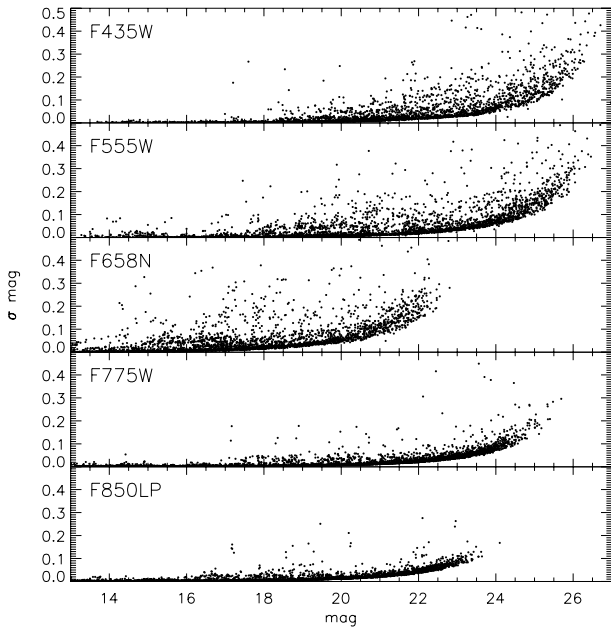
Figure 9. Photometric errors as a function of magnitude for the five ACS filters.

less affected by dust extinction—covered by these two other surveys.

Particular care has been used for close binaries, for which we checked the accuracy of the matching by comparing photometry estimate in different bands and relative stellar positions.

Having identified 1643 WFPC2 sources, we derived their photometry on the images corrected for cosmic rays. We extracted aperture photometry on both $0\rlap.{''}1$ and $0\rlap.{''}5$ radius apertures, corresponding to 5 and 11 pixels on WF1 and 2 and 5 pixels on WF2–4. The sky annulus was always taken between $1\rlap.{''}0$ and $1\rlap.{''}5$, corresponding to 20 and 30 pixels with WF1 and 10 and 15 pixels with WF2–4.

We applied CTE correction to the measured counts following the recipe of Dolphin (2000; also on http://purcell.as.arizona.edu/wfpc2_calib/). From the same source we adopted the zero points to the Vega system, using the values appropriate for a 14 $e^- \, \mathrm{ADU}^{-1}$ gain (updated on 2008 September 10). For the F336W and F656N filters, not included in Dolphin's list, we used the zero points on the WFPC2 Data Handbook, (http://www.stsci.edu/hst/wfpc2/analysis/wfpc2_photflam.html) applying the correction appropriate for 14 $e^- \, \mathrm{ADU}^{-1}$ gain. Their values (for the representative PC chip) are provided in Table 3.
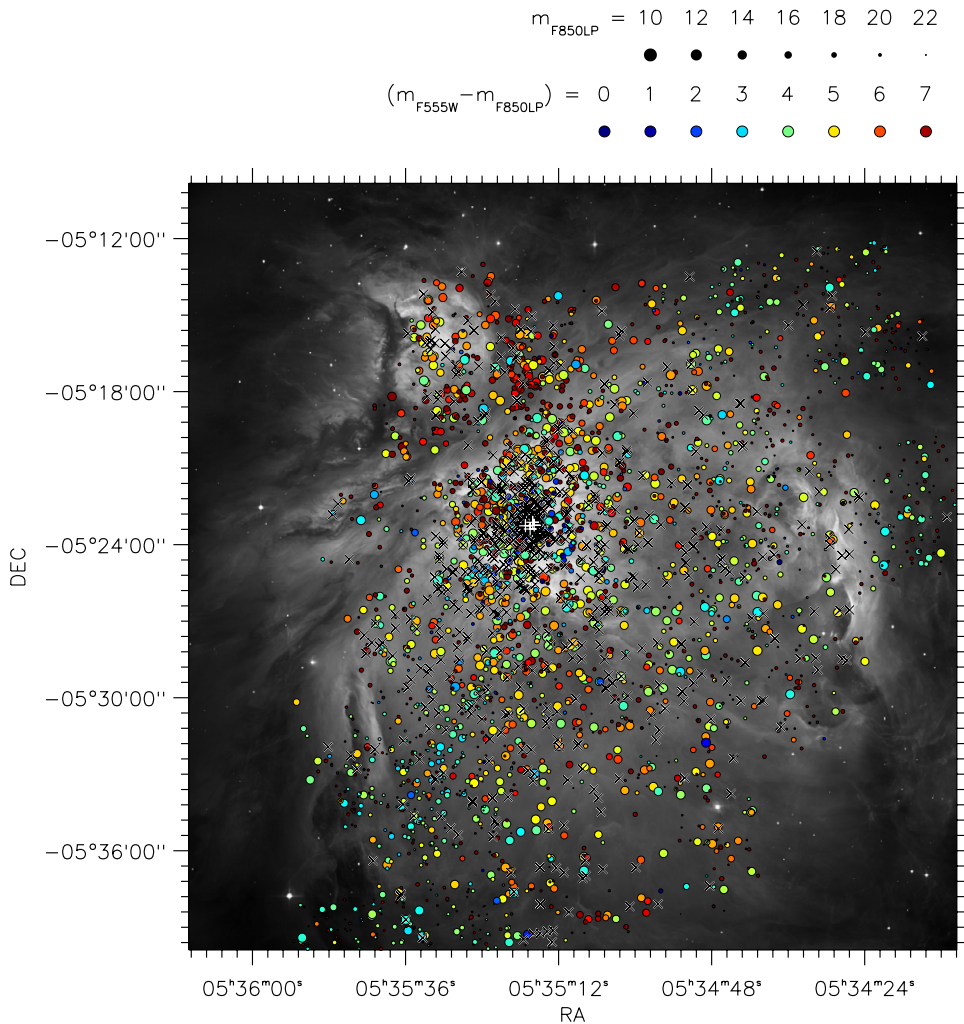
Figure 10. Spatial distribution of the sources in the ACS photometry, overlaid on the image of the Orion Nebula produced from the ACS imaging (see Section 6.1 and the Appendix). The stars are color coded according to their F555W–F850LP color as shown in the upper label; sources detected only in the F850LP are plotted using the reddest color of the label (7). The size of the circles relates to the luminosity of each star. Crosses indicate either saturated sources (+) or objects detected with low signal to noise ($\times$; S/N $\lesssim$ 3).

(A color version of this figure is available in the online journal.)

13
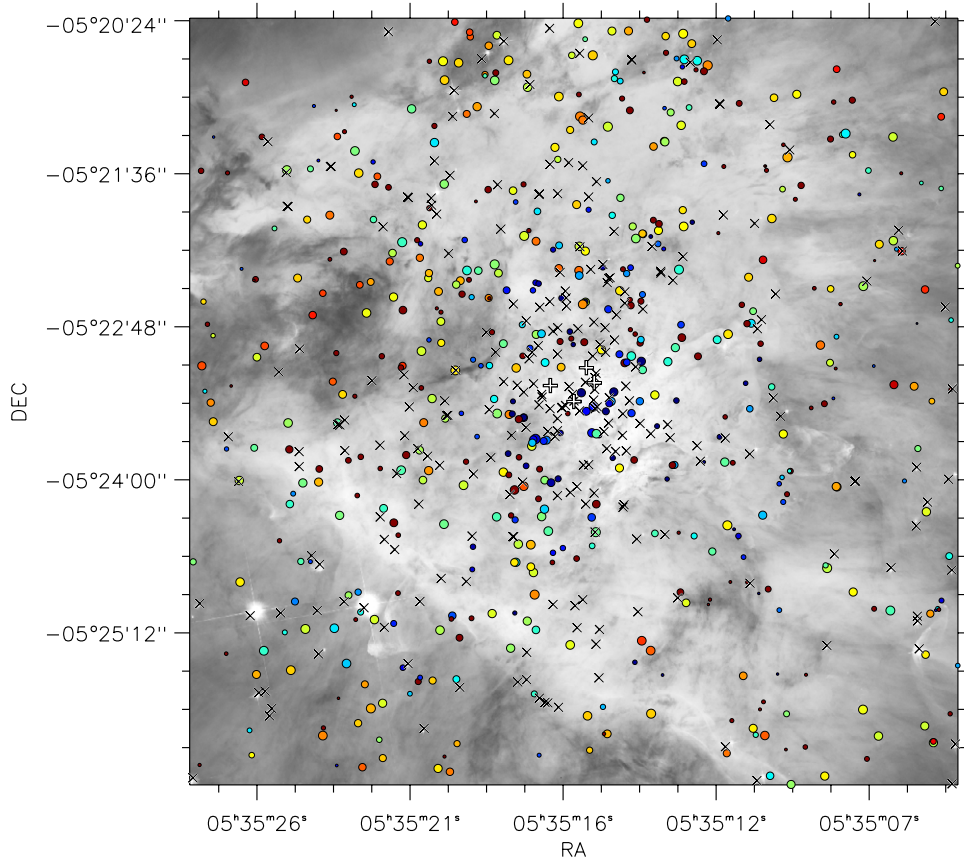
Figure 11. Same as Figure 10, for the inner part of the region.
(A color version of this figure is available in the online journal.)

The aperture correction from $0''.1$ to $0''.5$ was taken from Holtzman et al. (1995), appropriate for the WFCs. For the F656N aperture correction, not listed by Holtzman et al. (1995), we assumed the F675W values. Aperture correction between $0''.5$ and infinity was performed by subtracting 0.1 mag from the measured values, as appropriate for the adopted zero points. We added in quadrature the errors associated with the measured counts, zero point, CTE correction, aperture correction to infinity and, in the case of the $0''.1$ apertures, to the aperture correction to the $0''.5$ radius. This last term, when present, usually dominates, and for this reason, the $0''.5$ photometry is more accurate, except for the faintest sources detected in a few pixels. For the CTE correction, we assumed an error 20% of the amount of the correction itself.

In Figure 12, we present the calibrated magnitudes versus their corresponding errors for the 4 WFPC2 filters. Our 5σ sensitivity limits ($\sigma_{\mathrm{mag}} \simeq 0.2$) are about $m[\mathrm{F336W}] = 22.2$, $m[\mathrm{F439W}] = 21.7$, $m[\mathrm{F656N}] = 19.5$, and $m[\mathrm{F816W}] = 20.0$, in the Vega system. In Figure 13, we show the spatial distribution of the WFPC2 sources in the final catalog, color coded according to their color.

4.3. NICMOS Photometry

Source identification and photometry in NICMOS images are made difficult by the strong and non-uniform background emission, especially at the center of the survey area, and by the undersampled PSF of the NICMOS Camera 3. To remove the large-scale nebulosity, we applied a ring-median filter replacing each pixel with the median value taken in the surrounding annulus with inner and outer radii of 7 and 11 pixels
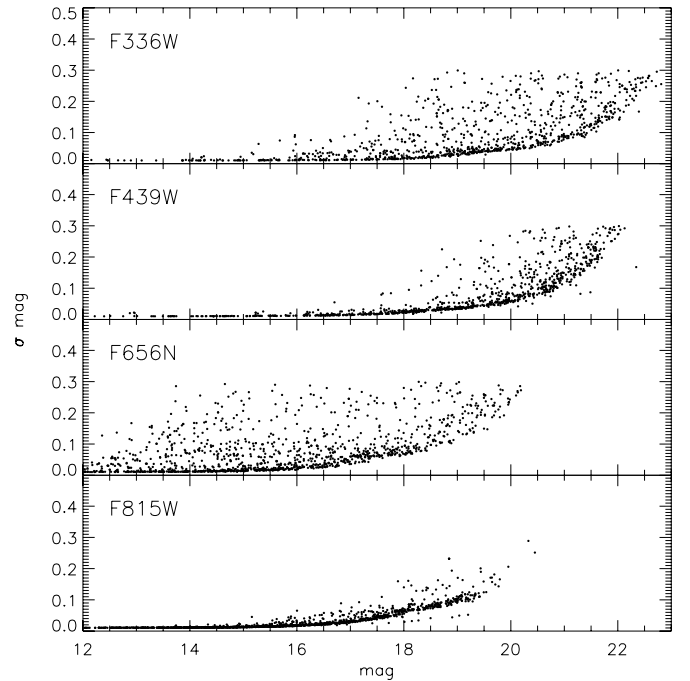
Figure 12. Photometric errors as a function of magnitude for the four filters used with WFPC2.

(corresponding to about $1''.4$–$2''.2$), respectively. The filtered image was subtracted from the corresponding original one to remove the large-scale nebulosity and enhance the detection of point sources.
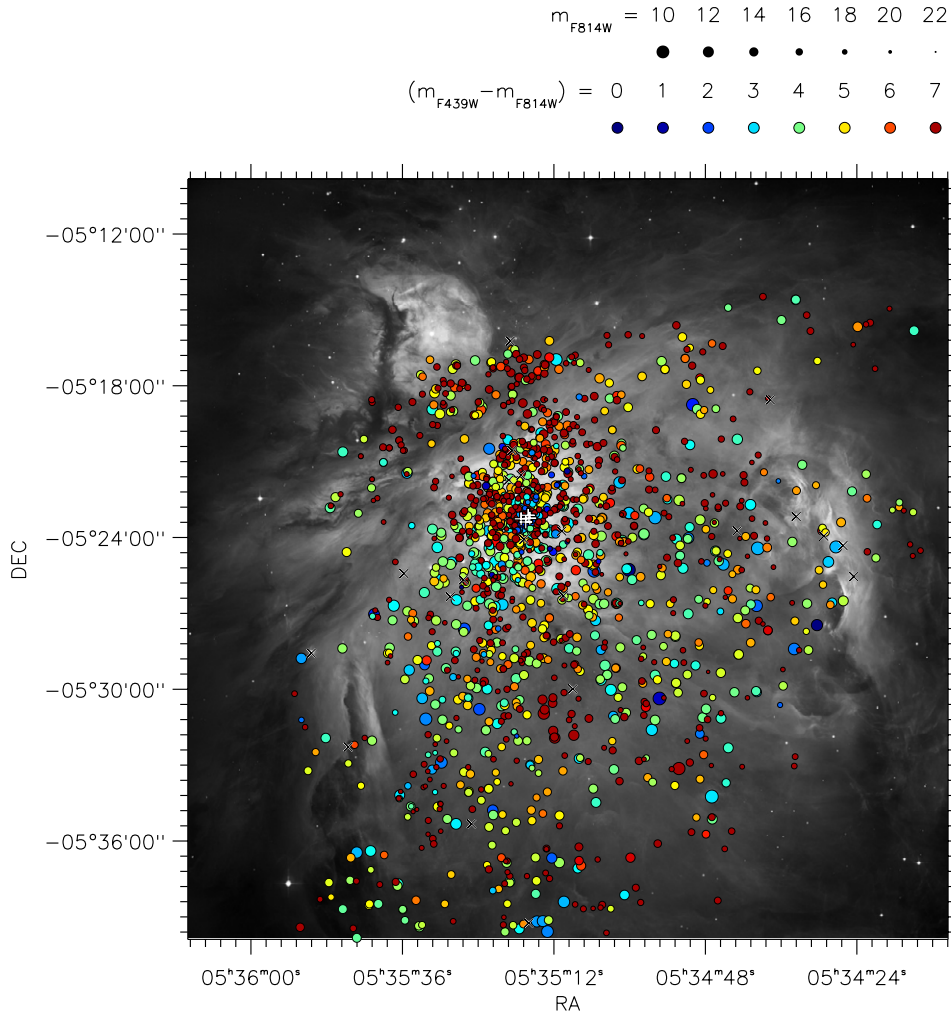
Figure 13. Same as Figure 10, for the WFPC2 photometric catalog.
(A color version of this figure is available in the online journal.)

Each point source was visually inspected in the F160W image, deeper than the F110W image and with better PSF sampling. The compatibility of the radial profile of each source with the typical PSF was also inspected to exclude spurious detections due to nebulosity. We detect a total of 2116 objects and used the positions of the objects in the F160W images to extract the photometry in both bands. Photometry was performed with an aperture radius of 2.5 pixels (0″.5) and a sky annulus between 10 and 15 pixels (2″.0–3″.0) for both filters. Bright isolated stars in different regions were used to determine aperture corrections with an estimated random error of 0.02 mag in both bands. The zero points, adopted from the NICMOS Data Handbook (Thatte et al. 2009) are 22.50 mag (F110W) and 21.66 mag (F160W) including aperture corrections.

Objects in common with 2MASS and with the ISPI near-IR survey of Robberto et al. (2010) were used to calibrate the astrometry of each mosaic. For visit 70, no reference star could be found within the field of view. Coordinates for the three sources in this field (entries 1389–1391, starting from 0) were obtained from the header information and are expected to be accurate to ≃1″, the average accuracy of the header coordinates derived from the other calibrated frames. NICMOS astrometry is generally in agreement with the ISPI astrometry to within 0″.1 for 60% of the sources and within 0″.2 for about 90% of the sources. Recently, Andersen et al. (2011) converted the photometric data into the 2MASS system using the ground-based data of Robberto et al. (2010). See their paper for a detailed discussion of how the completeness limit depends on the distance from the cluster center, and hence on the amount of nebulosity.

Figure 14 shows the photometric error for the NICMOS sources against the corresponding magnitudes, for both filters. Our photometry is significantly deeper than the previous ISPI study, reaching a 5σ limit (or about 0.2 mag of photometric error) of F110W $\simeq$ 20.7 mag, and F160W $\sim$ 20 mag. In Figure 15, we show the spatial distribution of the NICMOS sources in the final catalog, color coded according to their color.

5. DATA PRODUCTS

In this section we summarize the data products we have publicly released, available for download as High Level Science Products in the Multi-mission Archive at the Space Telescope Science Institute (http://archive.stsci.edu/prepds/orion/).

5.1. ACS

The ACS data set consists of three main products.

1. We provide the full set of 520 ACS *_flt.fits images, reprocessed according to version 5.1.1 of the CALACS pipeline, corrected for pixel area map and with reference celestial coordinates (CRVAL1 and CRVAL2 values in the
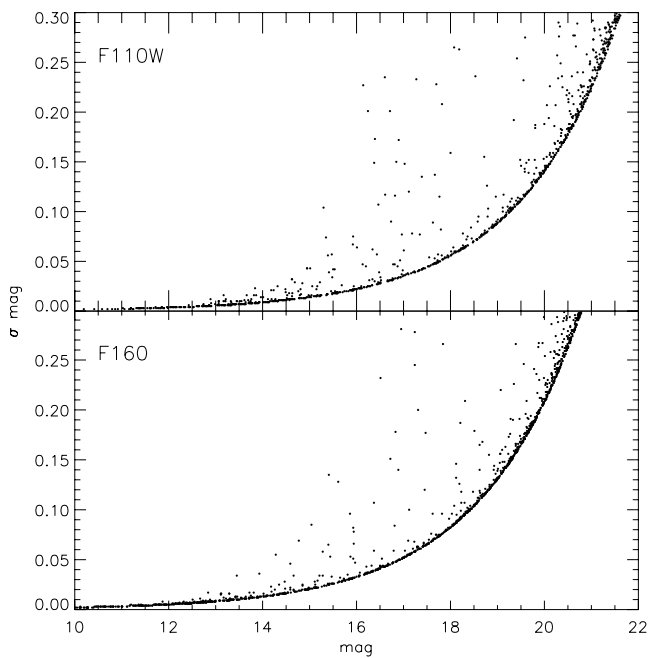
15

Figure 14. Photometric errors as a function of magnitude for the two NICMOS filters.

fits headers) registered to match the absolute astrometry of the stars falling in the field. Note that these images like every other *_flt.fits image released by latest version of the OTFR pipeline, contain simple image polynomial (SIP) coefficients for the correction of the field distortion. However, only the "direct" A_{nm}, B_{nm} coefficients are present, allowing us to directly derive the right ascension and declination corresponding to a certain pixel (using, e.g., the IDL *xyad* procedure), but not vice versa. As the reverse coefficients, Ap_{nm}, Bp_{nm}, are not present, the transformation from celestial coordinates to distorted pixel coordinates may require a different (e.g., iterative) approach.

2. We provide the full set of 90 ACS drizzled images, 9 strips per filter divided in left (east) and right (west) parts to maintain their image size below 1 Gpix. Their naming convention is strip#X_filter_drz.fits, where # refers to the strip number (0 to 8), X can be either L or R for the left or right part of each strip and *filter* is the ACS filter name. For the correspondence between visits (*_flt.fits files) and strips (*_drz.fits files), see Table 4. Note that the ACS drizzling software does not use the SIP coefficients but more refined distortion tables internal to the tool.

3. Finally, we provide the ACS source catalog with photometric data for 3399 stars. Of these, 352 have been measured once, 2074 twice, 249 three times, 682 four times, and 42
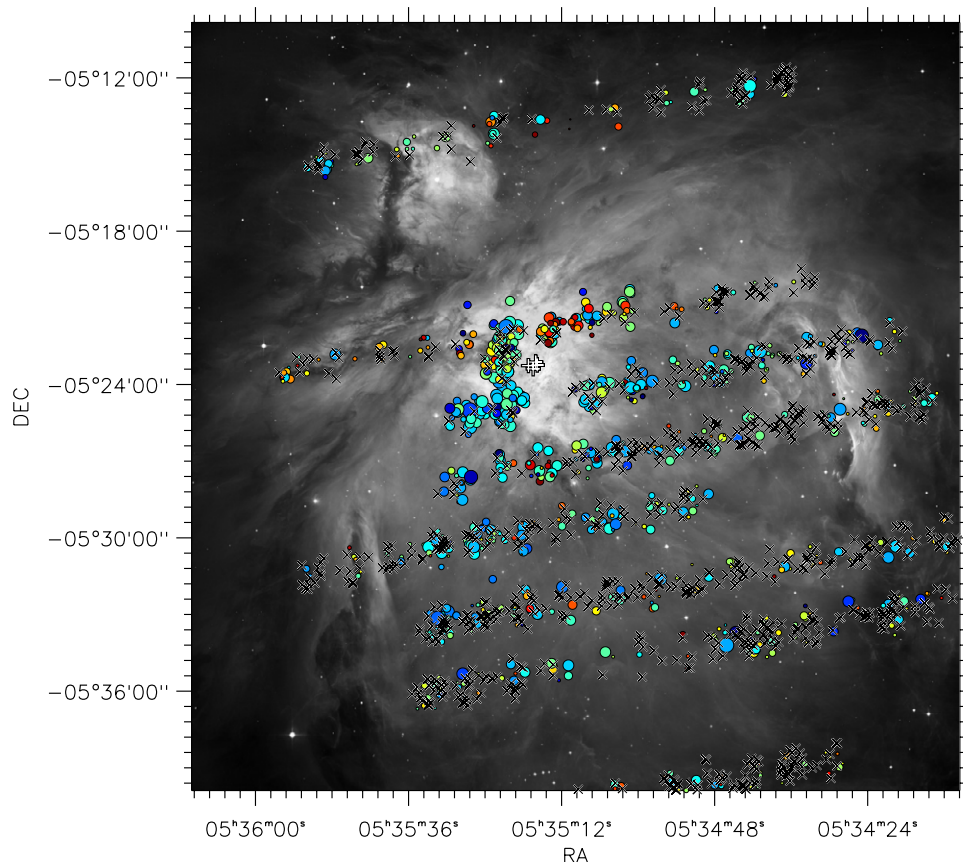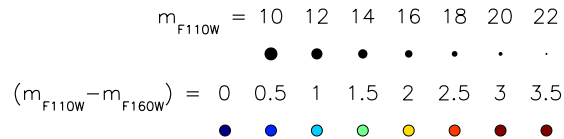
Figure 15. Same as Figure 10, for the NICMOS photometric catalog.

(A color version of this figure is available in the online journal.)

16

Table 5
ACS Source Catalog

Column	Description
onc_acs	Designation, or sequential entry number; identifies the observation of a source within a visit (orbit).
onc_acs_1	First entry number. This field facilitates finding sources observed multiple times. It provides the entry number (onc_acs) of the first appearance in the catalog. For example, entries onc_acs = 100, 101, and 102 are three observations of the same star (in different visits). They all have onc_acs = 100, as this is the first entry number attributed to this particular source.
x_435 to x_850	Five columns for the x positions measured in the *_flt.fits images, ordered by wavelength (F435W, F555W, F658N, F775W, F850LP). For saturated filters, the average on the unsaturated ones is used.
y_435 to y_850	Five columns for the y positions measured in the 5 *_flt.fits images.
m_435	F435W aperture photometry, in Vegamag, measured in the *_flt.fits image. If the star is undetected, this field takes the NULL value 99.9999; if saturated and not recovered, this value represents an upper limit.
dm_435	F435W aperture photometry error measured in the *_flt.fits image. If the star is undetect, this value represent the 3σ upper limit; if the star is saturated and not recovered, this field takes the NULL value 99.9999.
mf_435	F435W aperture photometry flag: 0 = undetected; 1 = detected; 2 = saturated and recovered; 3 = saturated and not recovered (upper limit); 4: undetected in the *_flt.fits image (flag = 0) but measured in the *_drz.fits strip.
m_555	Like the m_435 field for the F555W filter.
dm_555	Like the dm_435 field for the F555W filter.
mf_555	Like the mf_435 field for the F555W filter.
m_658	Like the m_435 field for the F658N filter.
dm_658	Like the dm_435 field for the F658N filter.
mf_658	Like the mf_435 field for the F658N filter.
m_775	Like the m_435 field for the F775W filter.
dm_775	Like the dm_435 field for the F775W filter.
mf_775	Like the mf_435 field for the F775W filter.
m_850	Like the m_435 field for the F850LP filter.
dm_850	Like the dm_435 field for the F850LP filter.
mf_850	Like the mf_435 field for the F850LP filter.
rad_435 to rad_850	Five columns, one for each filter, for the extraction radius for aperture photometry in *_flt.fits image, in pixels.
csky_435 to csky_850	Five columns, one for each filter, for the sky counts in aperture photometry in *_flt.fits image.
ssky_435 to ssky_850	Five columns, one for each filter, for the error of the sky counts in aperture photometry,in *_flt.fits image.
isky_435 to isky_850	Five columns, one for each filter, for the inner radius of sky annulus in *_flt.fits image, in pixels.
osky_435 to osky_850	Five columns, one for each filter, for the outer radius of sky annulus in *_flt.fits image, in pixels.
max_435 to max_850	Five columns, one for each filter, for the peak counts within extraction radius in *_flt.fits image.
spx_435 to spx_850	Five columns, one for each filter, for the number of saturated/bleeding pixels within the extraction aperture.
rspx_435 to rspx_850	Five columns, one for each filter, for the maximum distance of saturated pixels from the aperture center, usually along a bleeding trail, for each filter. If this value reaches 10 pixels, our maximum extraction radius, the star is considered saturated and is not recovered.
type	Source type, from visual inspection: (0) not measured; (1) detected in at least one filter and unresolved; (2) double (companion closer than $\approx$3 pixels, one entry for both sources); (3) wide double (companion further than $\approx$3 pixel, one entry for each source); (5) silhouette disk; (6) photoionized (proplyd or with other evidence of photoionization); (7) galaxy; (8) Herbig-Haro.
strip	*_drz.fits strip.
x_strip	x coordinate on *_drz.fits strip.
y_strip	y coordinate on *_drz.fits strip.
m_435s to m_850s	Five columns, one for each filter, for the aperture photometry in *_drz.fits strip. Null value 0.000 is used for sources non-measured.
dm_435s to dm_850s	Five columns, one for each filter, for the aperture photometry error in *_drz.fits strip. Null value 0.000 is used for sources non-measured.
rad_435s to rad_850s	Five columns, one for each filter, for the extraction radius for aperture photometry in *_drz.fits image, in pixels.
sky_435s to sky_850s	Five columns, one for each filter, for the sky counts per pixel in *_drz.fits image.
dsky_435s to dsky_850s	Five columns, one for each filter, for the error on sky counts per pixel in *_drz.fits image.
date	Date of observation (UT).
time	Time of observation (start of first exposure, F658N).

(This table is available in its entirety in a machine-readable form in the online journal. A portion is shown here for guidance regarding its form and content.)

five times, for a total of 8185 entries. Table 5 lists the entries provided for each star.

5.2. WFPC2

The WFPC2 data set consists of two main products.

1. The full set of 416 WFPC2 images (the pairs of F336W images being co-added), processed according to version 15.4c of the OPUS pipeline, corrected for pixel area map and with reference celestial coordinates (CRVAL1 and CRVAL2 values in the fits headers) registered to match the absolute astrometry of the stars falling in the field.

2. The WFPC2 catalog provides photometric data, at least in one band, for 1643 sources in total. Among these, 1592 were previously detected in the ACS survey and 51 only by ISPI. For 1021 stars (~60%), U-band photometry is available. Finally, for 897 sources (~55% of the total), we have photometry in all U, B, and I bands. For each of the 1643 stars listed in the WFPC2 catalog, we provide the entries listed in Table 6.

5.3. NICMOS

The NICMOS data set also consists of two main products.

1. The final drizzled images.

Table 6
WFPC2 Source Catalog

Column	Description
onc_wfpc2	Designation or entry number in the WFPC2 catalog.
onc_wfpc2_1st	First entry number. Like the similar field in the ACS catalog, this field facilitates finding sources observed multiple times by providing the entry number (onc_wfpc2) of the first appearance in the catalog.
RAh/RAm/RAs	Three columns for the hours, minutes, and seconds of right ascension (J2000.0).
DE-/DEd/DEm/DEs	Four columns (the first one for the sign) for the declination (J2000.0).
visit	Visit number
CCD	CCD detector of WFPC2; 1 is for the Planetary Camera, 2,3,4 are for the Wide Field Cameras.
x_336 to x_814	Five columns, for the four filters F336W, F439W, F656N, and F814W, for the x position on the chip
y_336 to y_814	Five column, one for each filter, for the corresponding y positions.
m_336	F336W magnitude (Vegamag).
dm_336	Magnitude error in the F336W filter.
mf_336	F336W aperture photometry flag: 0 = not measured; 1 = detected; 2 = non-detected; 3 = saturated.
m_439	F439W (B-band) magnitude (Vegamag).
dm_439	Magnitude error in the F439W filter.
m_656	F656N magnitude (Vegamag).
dm_656	Magnitude error in the F656N filter.
m_814	F814W (magnitude (Vegamag).
dm_814	Magnitude error in the F814W filter.
rad_336 to rad_814	Five column, one for each filter, for the aperture photometry extraction radius.
csky_336 to csky_814	Five column, one for each filter, for the sky counts for aperture photometry.
ssky_336 to ssky_814	Five column, one for each filter, for the sky counts errors for aperture photometry.
max_336 to max_814	Five column, one for each filter, for the source peak counts within extraction radius.
date	Date of observation (UT).
time	Time of observation.

(This table is available in its entirety in a machine-readable form in the online journal. A portion is shown here for guidance regarding its form and content.)

Table 7
NICMOS Source Catalog

Column	Description
ENTRY	Source ID number in the NICMOS catalog.
visit	Visit ID.
x	x-position on the drizzled NICMOS tile.
y	y-position on the drizzled NICMOS tile.
RAh/RAm/RAs	Three columns for the hours, minutes, and seconds of right ascension (J2000.0).
DE-/DEd/DEm/DEs	Four columns (the first one for the sign) for the declination (J2000.0).
m_110	Magnitude in the F110W filter. 99.9999 is NULL value.
dm_110	Magnitude error in the F110W filter. If m_110 = NULL this is an upper limit.
mf_110	Magnitude flag in the F110W filter. 0 = not measured, 1 = measured, 2 = undetected, with upper limit shown in dm_110.
m_160	Magnitude in the F160W filter. 99.999 is NULL value.
dm_160	Magnitude error in the F160W filter. If m_160 = NULL this is an upper limit.
mf_160	Magnitude flag in the F160W filter. 0 = not measured, 1 = measured, 2 = undetected, with upper limit shown in dm_160.

(This table is available in its entirety in a machine-readable form in the online journal. A portion is shown here for guidance regarding its form and content.)

2. The NICMOS source catalog, containing 2116 sources. The entries for each star are listed in Table 7.

5.4. Ancillary Ground-based Catalogs

As anticipated in Section 1, we have complemented our *HST* survey with ground-based observations at visible and near-IR wavelengths. The main purpose of these observations was (1) to measure sources that appeared saturated with the *HST*, given the relatively long exposure times we had adopted; and (2) to evaluate and minimize, as much as possible, the effect of source variability in the source colors, since the *HST* cameras did not observe the same field at the same time. For this reason, the observations were carried out on the same nights, 2005 January 1–2, using the Wide Field Imager (WFI) at the 2.2 telescope at La Silla for the optical survey and ISPI at the 4 m telescope at Cerro Tololo for the near-IR survey.

The optical observations, presented in Da Rio et al. (2009), have been taken in the *U*, *B*, *V*, *I* broadband, 6200 TiO medium-band, and Hα narrowband filters with the WFI imager at the ESO/MPI 2.2 telescope at La Silla Observatory. The source catalog contains 2612 point-like sources in the *I* band; 58%, 43%, and 17% of them are also detected in *V*, *B*, and *U* bands, respectively. There are 1040 sources identified in the Hα band. The near-IR observations, presented in Robberto et al. (2010), have been obtained in the *J*, *H*, and K_S filters. The catalog contains about 7800 sources, reaching 3σ accuracy in the 2MASS system down to $J = 19.5$ mag, $H = 18.0$ mag, $K_S = 18.5$ mag, enough to detect planetary size objects ($M \simeq 0.012\ M_\odot$) 1 Myr old under $A_V \simeq 10$ mag of extinction at the distance of the Orion Nebula, according to the Chabrier et al. (2000) models.
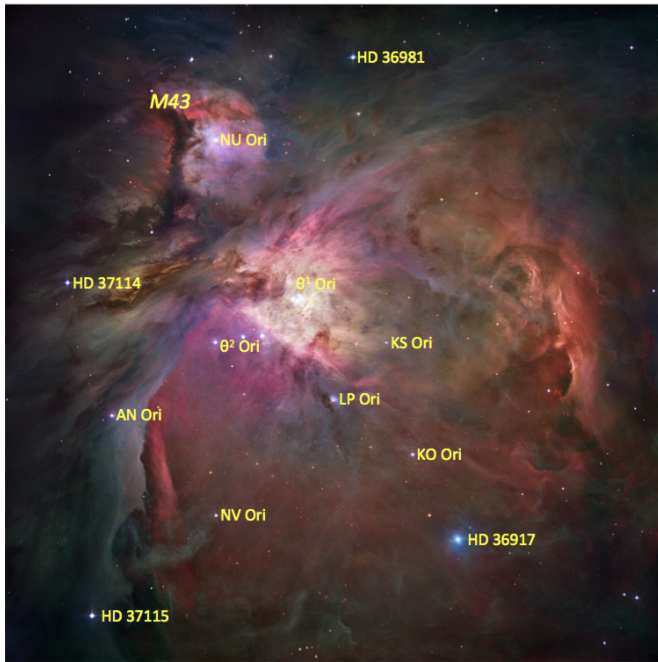
Figure 16. ACS color-composite image, together with the names of the main bright sources in the field of view.

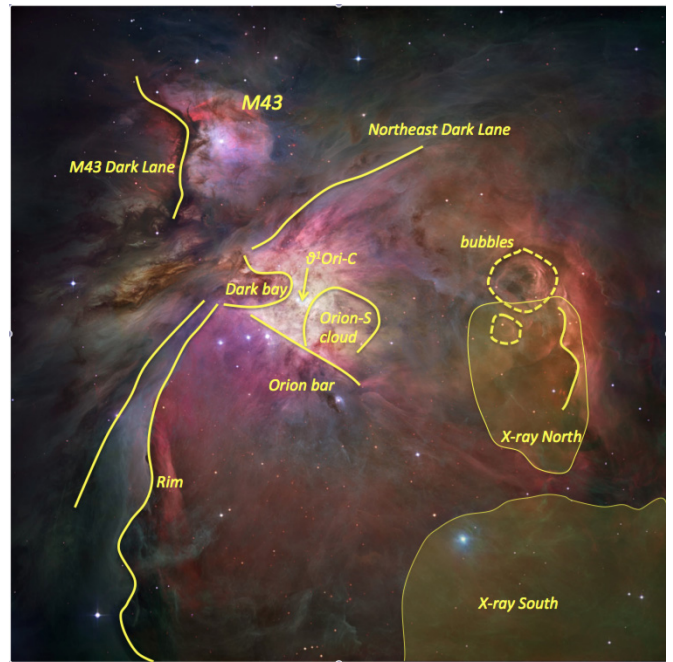(A color version of this figure is available in the online journal.)

Figure 17. Same as Figure 16, but indicating the principal nebular features of the Orion Nebula according to O'Dell & Harris (2010). See the text for details.

(A color version of this figure is available in the online journal.)

The images associated with these ground-based observations are also available as High-Level Science Product at the http://archive.stsci.edu/prepds/orion/. The tables with the photometry and derived physical quantities can be downloaded at no cost in machine-readable format from the electronic version of the publications or from the CDS archive: http://cdsarc.u-strasbg.fr/viz-bin/Cat?J/ApJS/183/261 for Da Rio et al. (2009), and http://cdsarc.u-strasbg.fr/viz-bin/Cat?J/AJ/139/950 for Robberto et al. (2010).

6. SELECTED RESULTS

In this section, we briefly illustrate some of the results obtained so far from our Treasury Program.

6.1. ACS Color-composite Image

One of the first products of our survey has been a multicolor image of the Orion Nebula. The image, available in both .pdf, .jpeg, and .tiff format with resolution up to $16,000 \times 16,000$ pixels, can be downloaded from http://hubblesite.org/gallery/album/pr2006001a. To facilitate comparison with other images and data sets, we have extracted the RGB planes of the $16,000 \times 16,000$ jpg image and converted them into FITS files adding basic astrometric information. They are available at the Web site http://archive.stsci.edu/prepds/orion. For accurate astrometric work, however, the drizzled strips at full resolution (50×50 mas) presented in this paper and available at the same site should be used. In the Appendix, we detail the complex image processing that has led to the production of the spectacular Hubble color image, shown in Figure 16 together with the names of the main bright sources in the field of view.

M42 is well known for its complex morphology. The historic reference for the naming of the major features, summarizing two centuries of early naked-eye observations, is Holden (1882). The wealth of data now available allows us to better understand

this region, in particular the inner few arcminutes ("Huygens region," see, e.g., O'Dell 2001a, 2001b; O'Dell et al. 2008). The Orion Nebula is a fossil cavity carved by the expansion of an H II region originally embedded within the Orion Molecular Cloud. The ionized blister has broken out of the molecular cloud at the current epoch, providing to our vantage point a low-extinction view of the cluster of young, forming stars. UV photons are still produced by the most massive stars, generating a photoionized wind streaming from the molecular cloud interface and filling the cavity. O'Dell & Harris (2010) provide the most up-to-date model of the large structure of the nebula, based on the combined analysis of images and spectroscopy of emission lines from multiple ions of various ionization potential energy. In Figure 17, we illustrate some of the most prominent features discussed by O'Dell & Harris (2010). In particular: (1) the "Bright Bar" and escarpment of the ionization front nearly edge-on with respect to our vantage point; (2) the Orion South region, an active site of star formation identified as a dense cloud in front of the main ionization front (O'Dell et al. 2009); and (3) the M43 region around the B1V star NU Ori, separated from θ^1Ori-C by the optically thick northeastern dark lane. Figure 17 also shows the approximate location of the two extended X-ray emitting regions discovered by Güdel et al. (2008) and the outline of a couple of remarkable circular structures ("bubbles") at the eastern side of the region. An earlier 3D reconstruction of the Orion Nebula has informed the production of the "fly-by" animation included in the award-winning *Hubble 3D* IMAX® 3D documentary.[21]

6.2. Color–Magnitude Diagrams

Color–color and color–magnitude diagrams allow us to isolate stars with anomalous properties, like extreme blue colors, due either to light scattered off the disk or emitted by accretion, as well as foreground objects with very low reddening. In Figure 18 we present the z versus ($I - z$) color–magnitude
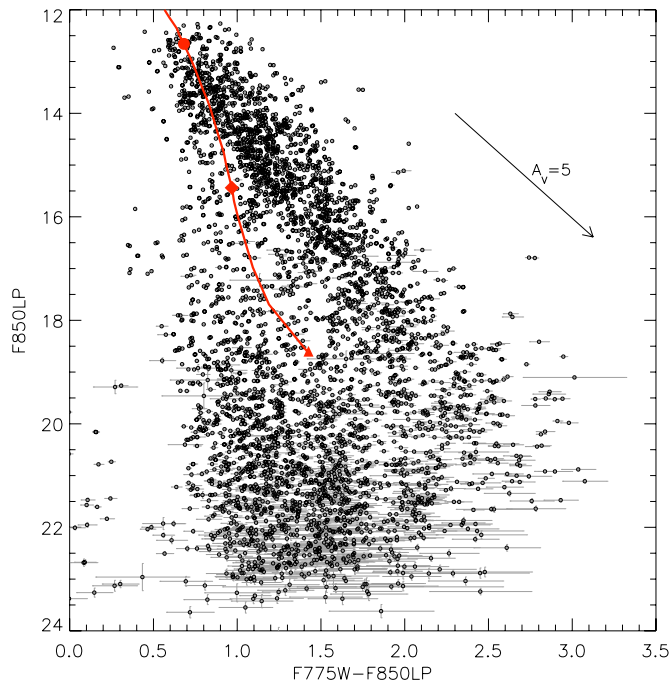
---

[21] http://www.imax.com/hubble/

Figure 18. z vs. $(i-z)$ color–magnitude diagram from our ACS photometry. The red line represents a Baraffe et al. (1998) 1 Myr isochrone for $A_V = 0$. Along this line, the circle marks a mass of 0.5 $M_\odot$, the diamond symbol represents the H-burning limit ($M = 0.08\ M_\odot$), and the triangle represents $M = 0.02\ M_\odot$. The arrow indicates a reddening vector of $A_V = 5$ mag, assuming the extinction law of Cardelli et al. (1989).

(A color version of this figure is available in the online journal.)

Figure 19. Same as Figure 18, but using the NICMOS photometry (F110W vs. F110W–H160W).

(A color version of this figure is available in the online journal.)

diagram, which shows the clear separation between the young ONC sequence (the diagonal distribution of source located mostly above the isochrone) and the background population (the population of data points below the isochrone. The ONC stars are distributed along the reddening direction, the density of points tracing the luminosity function, and therefore the IMF, of the cluster. The same diagram made for the NICMOS filter (Figure 19) shows a much less distinct PMS locus, presumably because the IR filters penetrate better into the molecular cloud, yielding stellar members with a wider range in A_V. In both Figures 18 and 19 we also display a theoretical PMS isochrone. This is a 1 Myr isochrone from Baraffe et al (1998), converted in *HST* magnitudes through synthetic photometry assuming model spectra from Allard et al. (2012). The isochrone is merely shown for illustrative purpose, to highlight the depth of our photometric survey, reaching well down to planetary masses. It is well known that both evolutionary models and synthetic spectra are somewhat inaccurate in the very low mass star and brown dwarf regimes, and they should be calibrated empirically before deriving stellar properties from the observed quantities. For the analysis of the NICMOS data set and the derivation of the NIR IMF, we refer to Andersen et al. (2011); see also Section 6.4.

6.3. Circumstellar Disks and Proplyds

The excellent angular resolution of our *HST* survey allows us to resolve a large number of protoplanetary disks in Orion. Ricci et al. (2008) used the ACS images to obtain a census of all of such objects detected in our ACS imaging survey. The list counts 178 externally ionized protoplanetary disks (*proplyds*; O'Dell & Wen 1994), 28 disks seen only in absorption against the bright nebular background (*silhouette disks*), 8 disks inferred from the presence of an opaque mid-plane between extended
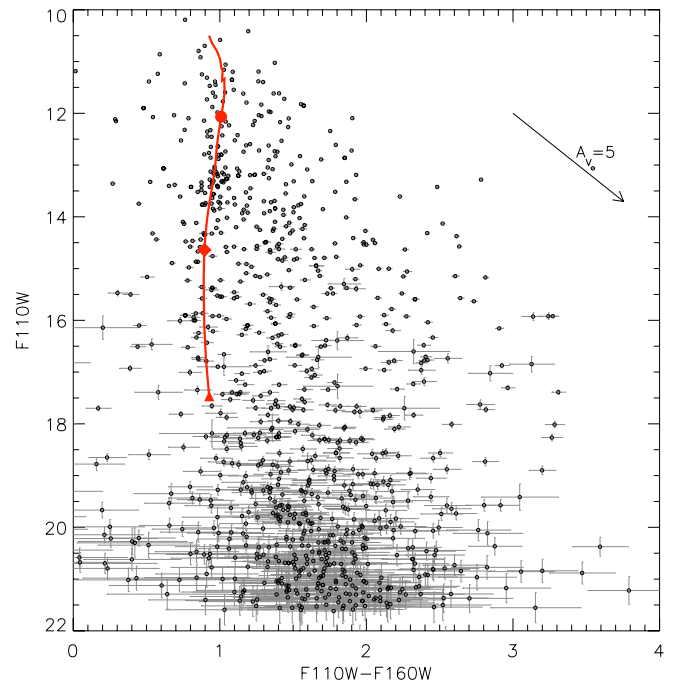
bipolar emission (*bipolar nebulae* or *reflection nebulae*), and five sources showing jet emission with no direct evidence of disk (either as a dark silhouette or through photoevaporated emission). As usual, many of these disks are associated with jets seen in Hα and/or circumstellar reflection emission seen in broadband filters. The work of Ricci et al. (2008) also resulted in an ESA Press release (heic0917).[22] A color-composite ACS image of a sample of disks is presented in Figure 20.

Using ACS data, two disks have been studied in detail. Robberto et al. (2008) have analyzed the photoionized proplyd 124–132. This remarkable systems appears as a photoevaporated disk surrounding a two point-like sources separated by 0″.15, or about 60 AU at the distance of Orion. The authors show that the luminosity and colors of the sources are compatible with a pair of objects of similar substellar mass ($\simeq 0.04\ M_\odot$) and about 1 Myr old. On the other hand, more massive stars under a large amount of extinction could also explain the observed fluxes; spectroscopic confirmation is needed to disentangle the two cases. In any case, this system represents the first direct observation of a circumbinary disk undergoing photoevaporation. The second system investigated in detail is the well-known dark silhouette disk 114–426 (Miotello et al. 2012). The high signal-to-noise ratio of the ACS images has allowed us to clarify the complex morphology of the system and unveil evidence of photoevaporation. By comparing the opacity of the outer regions at different wavelengths, the authors have reconstructed the distribution of dust grains, finding evidence for large (micron size) grains with a spatial gradient compatible with a photoevaporative wind.

6.4. Other Studies

Our accurate multi-band photometry for thousands of ONC stars provides a unique data set for studies of this young

---

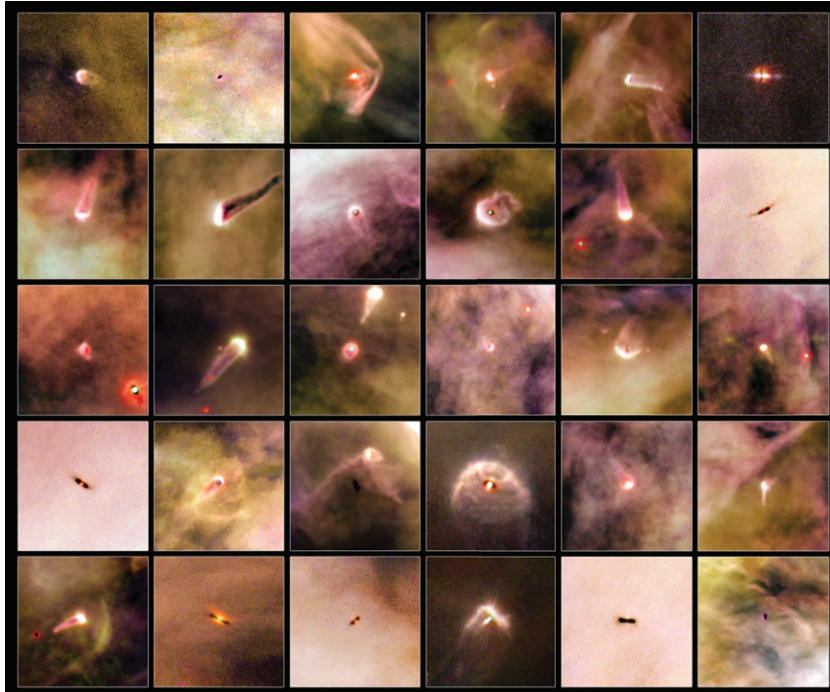[22] Available at http://www.spacetelescope.org/news/heic0917/

Figure 20. Beautiful collection of protoplanetary disks in the ONC observed in our ACS imaging. In many cases, they appear externally photoionized. Images are adapted from Ricci et al. (2008) and the ESA Press Release heic0917 (Image credit: NASA, ESA, and L. Ricci, ESO).

(A color version of this figure is available in the online journal.)

population. In the past few years preliminary photometry has been utilized for a number of investigations. In this section we highlight the main ones. Da Rio et al. (2009, 2010) used the WFI ground-based optical photometry obtained with the MPG-ESO 2.2 m telescope in La Silla as a follow-up to the *HST* Treasury Program to study the stellar population of the ONC down to 0.1 $M_\odot$. In these works, the ACS photometry was used to estimate the photometric completeness of the ground-based data, given the significantly deeper detection limit of the *HST* survey. The second paper presents a new version of the Hertzsprung–Russel diagram of the cluster first derived by Hillenbrand (1997). The new estimates of stellar masses and ages indicate a peak age of ∼2–3 Myr and a flattening or turnover of the IMF at about 0.2–0.3 $M_\odot$. Recently, Da Rio et al. (2012) have used new WFI data to expand this study into the substellar regime.

A more detailed analysis of the age spread of the ONC, using the ACS data presented in this paper, has been performed by Reggiani et al. (2011). Using the Bayesian analysis tool Chorizos (Maíz-Apellániz 2004), they estimate the extinction and accretion luminosity toward each source. From the isochronal ages, accounting for all major sources of uncertainty through Monte Carlo modeling, they derive a mean cluster age of 2.2 Myr with a spread of few Myr, inconsistent with that of a coeval stellar population and in agreement with a star formation activity lasting between 1.5 and 3.5 Myr.

The NICMOS data were used by Andersen et al. (2011) to determine the ratio of low-mass stars to brown dwarfs as a function of radial distance, out to about 1.5 pc. The comparison with the results previously obtained for the central 0.3 pc × 0.3 pc region suggests that the fraction of low-mass members of the cluster is mass segregated.

Following an early study of the ONC core by Robberto et al. (2004), who used WFPC2 data to derive accretion rates $\dot{M}$ in the core of the ONC for 40 stars, Manara et al. (2012) analyzed the new WFPC2 photometry to derive the mass accretion rate for ∼700 cluster members using both the *U*-band excess and Hα emission. This is the largest sample of nearly coeval PMS sources to date for which $\dot{M}$ has been derived, and has allowed us to perform the most complete statistical study of the final phases of the stellar mass buildup. The data show trends between the mass accretion rate, and the age and mass of the sources, with a mass accretion rate decaying more rapidly for lower stellar masses.

Two studies used the data set presented in this paper to analyze the proper motion of selected sources. O'Dell et al. (2005) used the ACS and WFPC2 images as a second epoch, together with previous *HST* observations of the ONC, to measure proper motions of three stars, JW 349, JW 355, and JW 451, that had been reported as high-velocity low-mass runaway stars. The combination of *HST* data does not show evidence of significant proper motion. Henney et al. (2007) also used our *HST* images, together with high-resolution spectra and radio maps, to study the nature of optical outflows in the vicinity of the Orion South region.

The combination of the *HST* data with those obtained by other great observatories like *Chandra* and *Spitzer* is still in an early phase. Prisinzano et al. (2008) used the X-ray *Chandra* Orion Ultradeep Project (COUP) survey (Getman et al. 2005) to select 41 Class 0–Ia candidate sources. The data from our *HST* Treasury Program were used to trim the list by removing the objects detected at visible wavelengths. The authors find that Class 0–Ia objects appear to be significantly less luminous in X-rays than the more evolved Class II stars with mass larger than 0.5 $M_\odot$. Aarnio et al. (2010) used the ACS and WFI fluxes, together with 2MASS and *Spitzer* IRAC+MIPS fluxes, to model the spectral energy distributions (SEDs) of the 32 most powerful X-ray flaring sources from the COUP (Getman et al. 2005). They were able to determine for each star the location of the inner edge of the circumstellar disk relative to the corotation distance
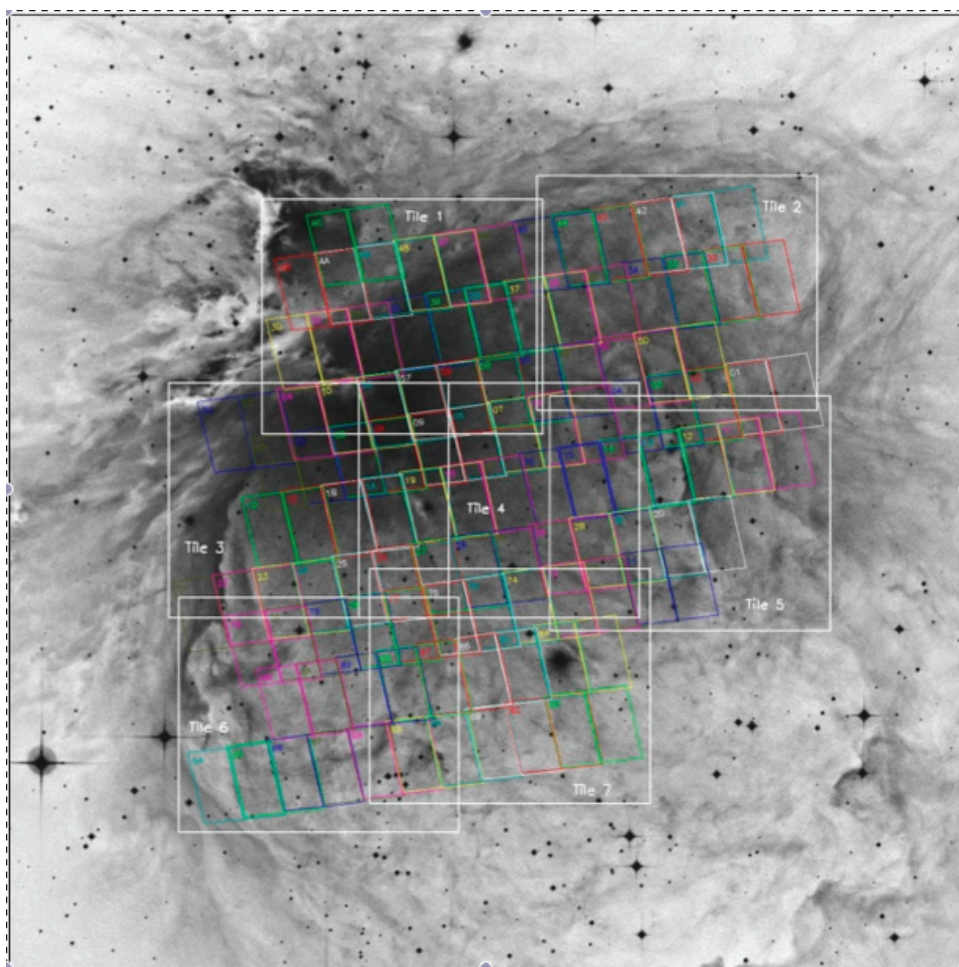
Figure 21. Distribution of 104 ACS fields on the sky and outline of the seven primary tiles used for the production of the *HST* image, superimposed on an AAT image of the Orion Nebula (David Malin Images). The primary tiles (white rectangles) represent the results of initial data reduction, seven equal-sized tiles of $13,000 \times 14,000$ pixels, or 174 Mpix.

(A color version of this figure is available in the online journal.)

from the star, based on each star's known rotation period from Stassun et al. (1999). In most cases, the large magnetic loops are not anchored to the circumstellar disks, but appear as free-standing magnetic structures.

The scientific potential of the data set presented in this paper still has to be fully mined. Our team is working on the analysis of the sample of binary sources, the accurate reconstruction of individual SEDs, and on the multicolor study of other prominent proplyds. Also the matching of the *HST* data with other data sets, both from *Spitzer* and *Chandra* and ground-based telescopes relative, e.g., to radial velocity, proper motions, and source variability will provide unique information on the structure and evolution of the ONC and PMS evolution in general. By making the entire data set available to the community we hope to stimulate research in these directions.

7. CONCLUSION

In this paper, we have presented the observing strategy, data analysis, data products, and a summary of the scientific results obtained by the *HST* Treasury Program on the ONC (HST GO-10246, PI: M. Robberto). The survey, carried out simultaneously with all *HST* imagers (ACS, WFPC2, and NICMOS), probed the PMS population of the ONC down to masses of the order of 1 Jupiter mass. The finally reduced images and the photometric databases, including the complementary

ground-based data obtained at La Silla and Cerro Tololo, are available to the community as high-level data products on the Multimission Archive hosted by the Space Telescope Science Institute (http://archive.stsci.edu/preds/orion/).

APPENDIX

PRODUCTION OF THE *HST* IMAGE

The set of ACS images presented in this paper has been used to obtain the most detailed images of the Orion Nebula to date.
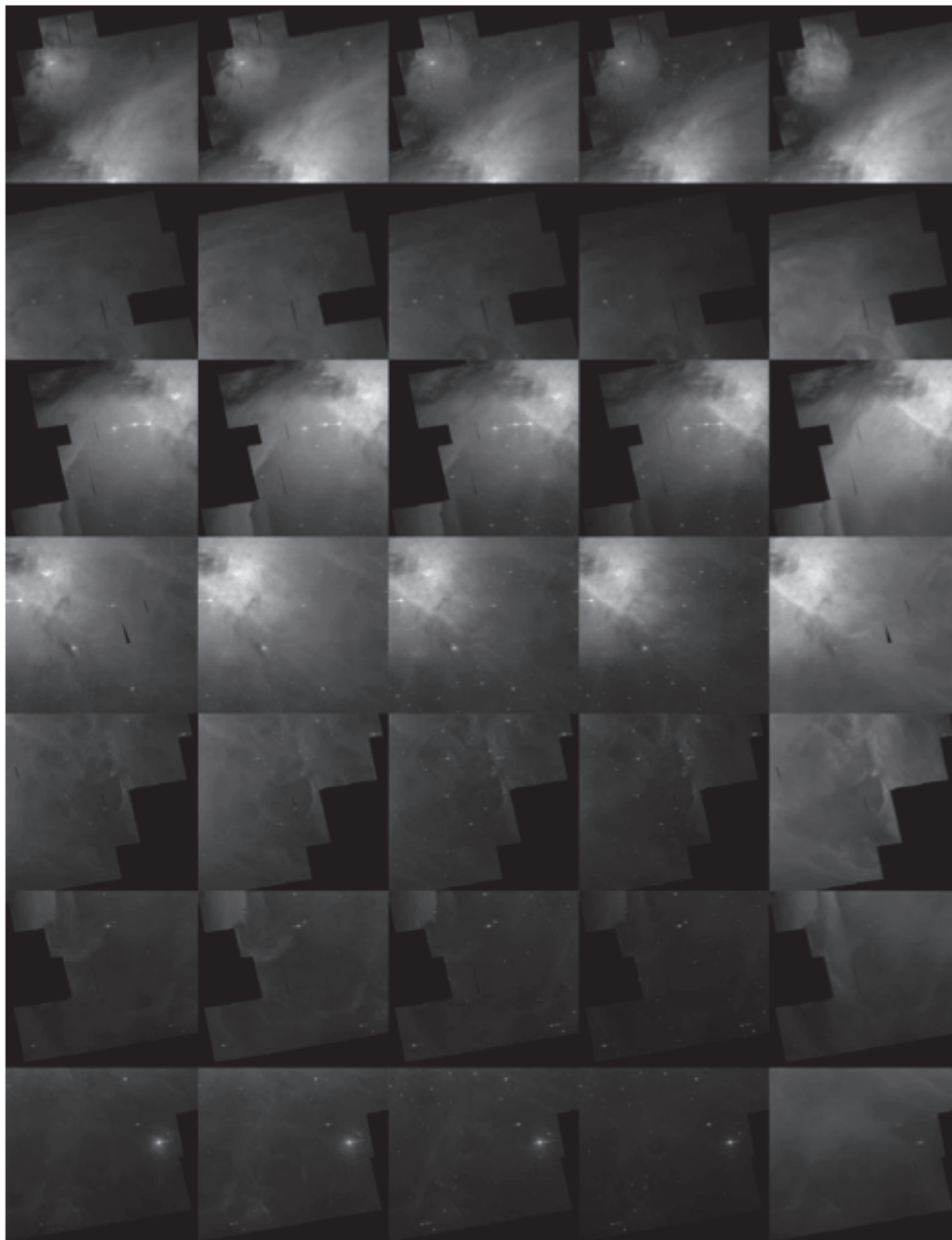
Figure 22. Images resulting from initial intensity scaling to 16 bit, gray, flat Photoshop documents, each $13,000 \times 14,000$ pixels (174 Mpix). Images in each row represent data from the five different filters, left to right: B, V, i, z, and Hα. Images in each column represent the initial tiles from each filter.

We describe here the process of producing a color-composite image from the assembled *Hubble* data for distribution to the public, media, and astronomers.

Working with over one billion pixels of high dynamic range ACS data presented practical challenges. An equivalent challenge was producing an image distinct from the gallery of existing photographs of this popular target, but not so unusual as to appear unrealistic. Compromises were necessary to achieve a result with an unwieldy volume of data and subjective choices, made for largely aesthetic reasons, were needed to arrive at the final product. The entire process was carried out in collaboration with the science team, keeping in mind a set of main goals: (1) produce a visually striking image, with (2) realistic overall appearance, tonality, and color, (3) render coolest stars red, hottest stars blue, (4) represent the broad dynamic range in

the data, (5) render detailed structure present in the data, and (6) stay honest to the data.

The data used as input were the seven overlapping tiles, each $13,000 \times 14,000$ pixels (174 Mpix) mentioned in Section 3.3 and shown in Figure 21. This amounts to 35 FITS files, 1.35 GB each. Fully assembled, accounting for overlap and some margin, they correspond to $32,567 \times 35,434$ pixels or 1.1 Gpix.

The remainder of this report explains these procedures in somewhat more detail.

A.1. Intensity Scaling of Each Tile/Filter

The first step was to scale each of the 35 input files into an editable, 16 bits per channel (bpc) image. Since the ACS data
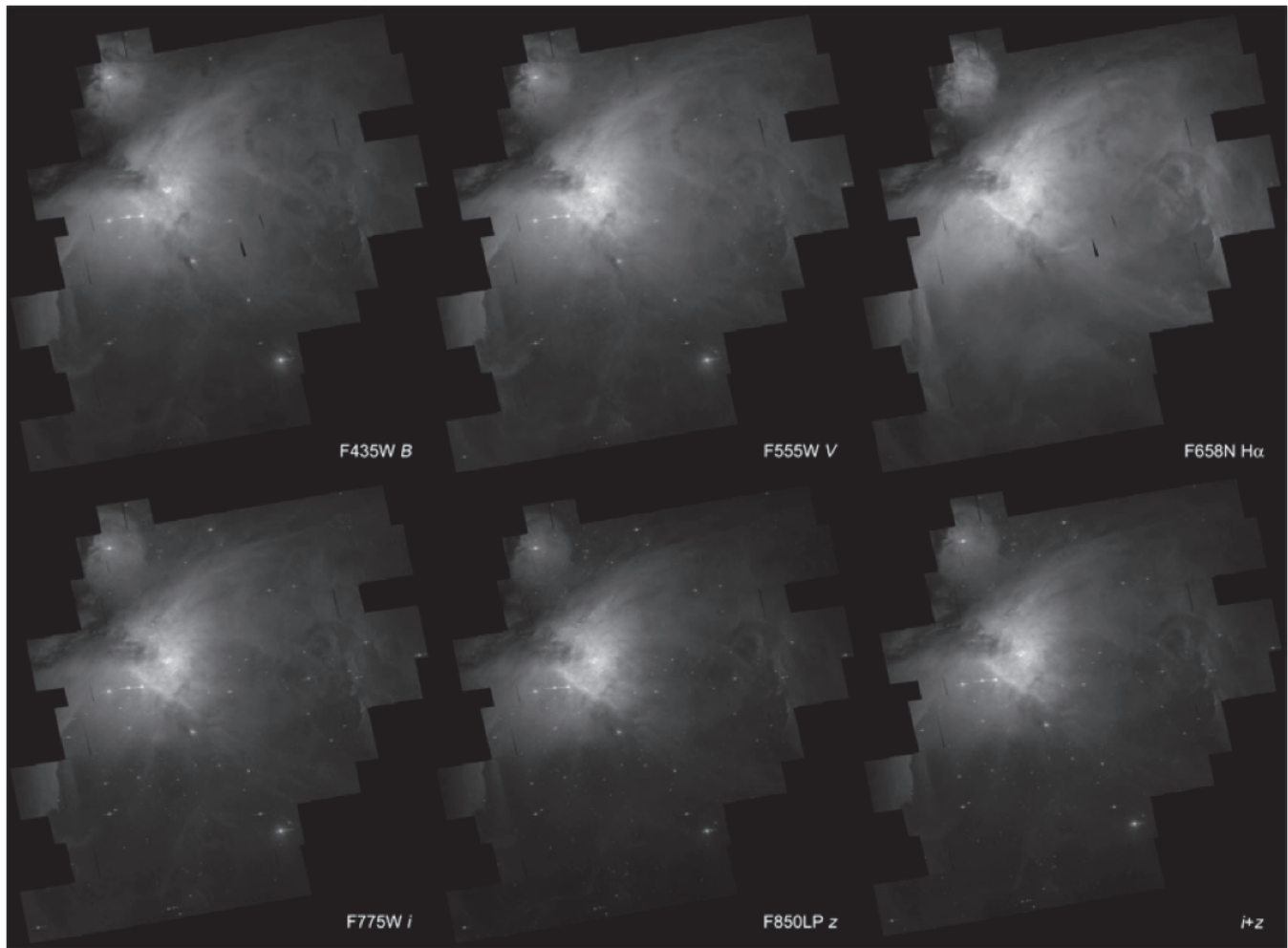
Figure 23. Images retiled for each filter, 16 bit, gray, flat Photoshop documents, each $32{,}567 \times 35{,}434$ pixels (1.1 Gpix).

Figure 24. Initial color-composite image including only *HST* ACS data, 16 bit RGB $32{,}567 \times 35{,}434$ pixels (1.1 Gpix).

(A color version of this figure is available in the online journal.)

Table 8
Assigned Colors to Produce the Color-composite Image

HST ACS Filter	ESO Filter	Assigned Color
F435W *B*	F435W	Blue
F555W *V*	F555W	Green
F775W *i*+F850LP *z*	[S II]	Red
F658N Hα	Hα	Orange

were processed and calibrated consistently, the same intensity-scaling parameters could be used for each tile and filter. Parameters were adjusted to produce a wide, smooth range of tones, with detail apparent in the brightest (highlight) and darkest (shadow) regions across all of the images (Figure 22).

A.2. Retile of the Full Mosaic

The next step converted each set of the seven 16 bpc tiles, one set for each filer, into a single mosaic. The image size had to be reduced by a factor of two in each dimension because hardware and software limitations prevented working with the full-size, 16 bit images. While there was a strong desire to keep the image at the native pixel scale ($0\rlap{.}''050$ pixel^{-1}), it soon became clear that this would have been highly impractical, given the state of the art in desktop processing at the time and the size of the full-scale image, $36{,}000 \times 36{,}000$ pixels or some 1.2 Gpix. Given the additional overhead of multiple image and adjustment
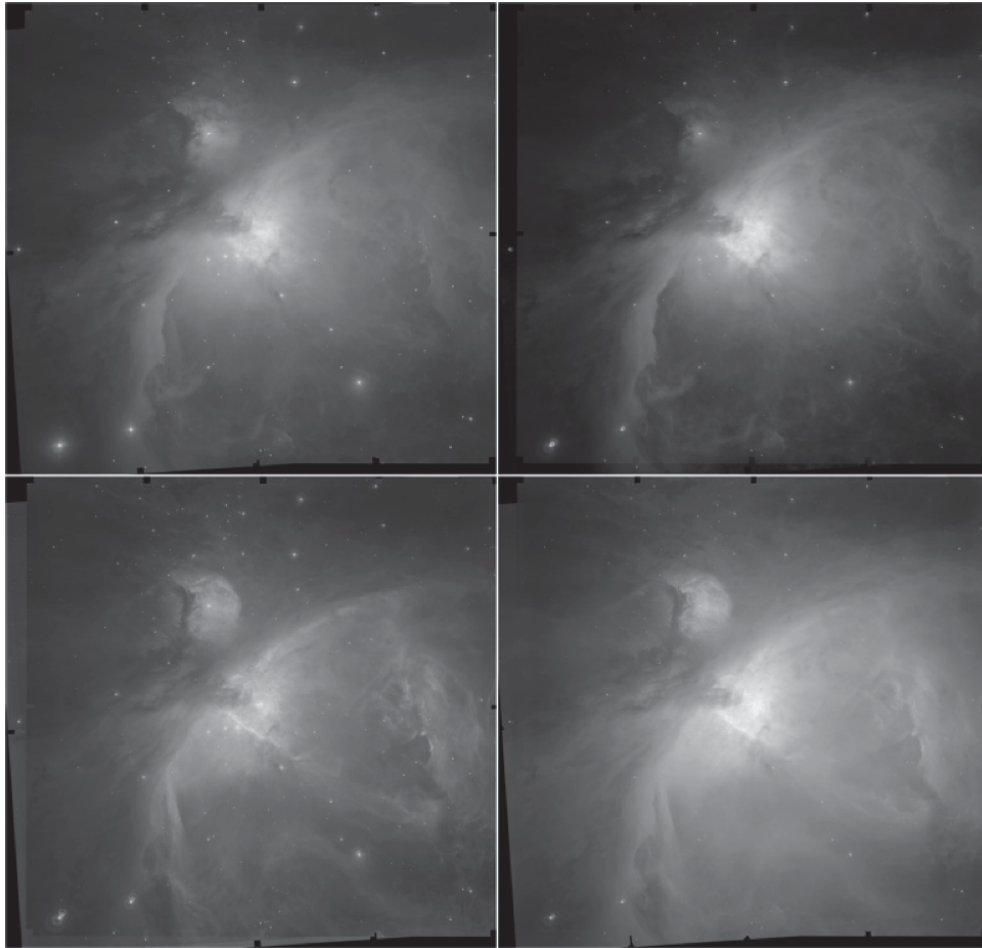
Figure 25. Scaled MPG/ESO 2.2 m WFI (ground-based) images, top-left: B; top-right: [O III], bottom left: [S II], and bottom-right: Hα, 9064 × 8726 pixels (75 Mpix).

Figure 26. Left: *HST* ACS Hα mosaic, center: mask to blend with ground data, and right: scaled ESO Hα image.
(A color version of this figure is available in the online journal.)

layers, masks, etc., for image editing, anything larger than a ≃16,000 × 16,000 pixel proved prohibitive (Figure 23).

The most straightforward way to reconstruct a color image assigns different images to the three additive primary color channels, red, green, and blue. However, it is possible to make a color composite with more than three constituent images using a layering paradigm to assign hue to individual grayscale images. After testing various combinations of filters and color assignments, the two reddest filters, F850LP and F775W were averaged into a single image. The final color adjustments were: F658N was rendered in red/orange, F850LP+ F775W in red, F555W in green, and F435W in blue (see Table 8 and Figure 24).

A.3. Combine with Ground-based ESO Data

The next step was the matching with ground-based data. This was necessary because the ACS survey was not designed to fill out a rectangular pattern. The combination of stripes resulted in a mosaic with ragged edges and a few interior gaps. We felt that a clean, rectangular composition would be more appropriate for a public presentation of the image, as the irregular edges would strongly distract viewers from the primary subject and finely detailed structure of the image. The science team provided another set of data in five filters: together with the WFI *U*-band Hα data presented by Da Rio et al. (2009), we used two unpublished images also taken at the MPG/ESO

Figure 27. Left: initial composite including both ACS and ESO data; center: result after applying brightness, contrast, and color balance adjustments; right: cumulative effect of adjustments and masks on a constant, gray image to illustrate smoothness of the adjustments applied based on the smoothed image brightness.

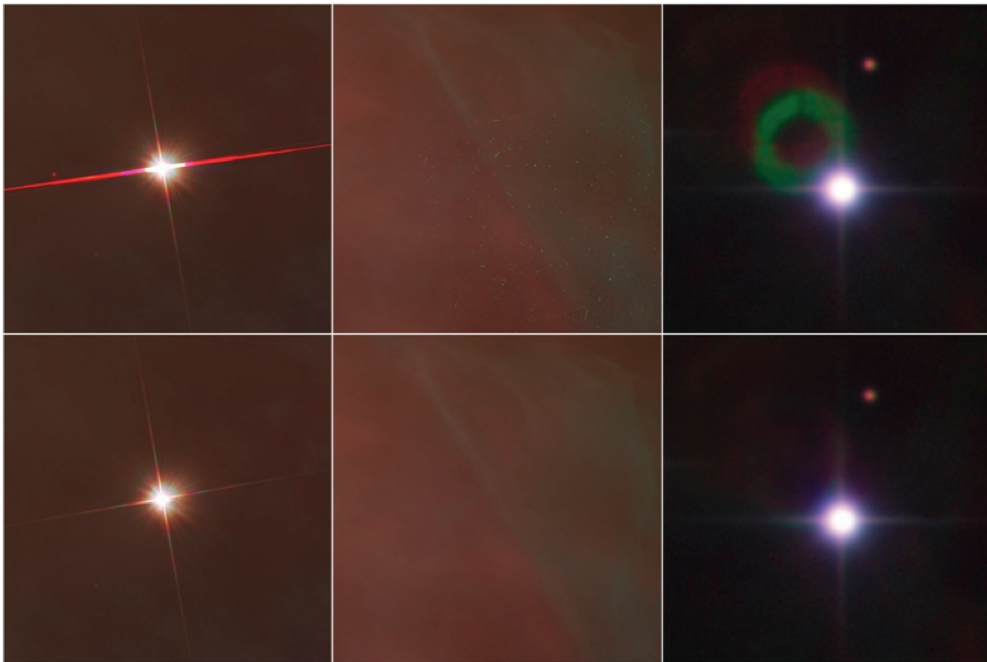(A color version of this figure is available in the online journal.)

Figure 28. Examples of cosmetic retouching on small sections of the adjusted color-composite mosaic. Top: three examples of observational artifacts: CCD charge bleed, residual cosmic rays, and internal reflections. Bottom: retouched versions of the same image sections.

(A color version of this figure is available in the online journal.)

Figure 29. Result of final adjustments. The intent was to enhance contrast throughout the image to make a crisper rendition but without sacrificing highlight or shadow detail, nor an overall sense of the very large range of brightness inherent in the data.

(A color version of this figure is available in the online journal.)

2.2 m telescope, one in sulfur ([S II]) and the other in the oxygen ([O III]) filter. These images matched closely enough the passbands of their closest ACS filters (Figure 25).

The *HST* data were then scaled from the full-dynamic-range FITS into 16 bit images. Slightly different scaling parameters were used for each image, though a logarithmic transformation was used for all. The goal was to balance shadow and highlight values with a consistent tonal range among the four images used. The scaled ESO data were finally combined with the *HST* data scaled at the ESO pixel size, 16 bits, separately for each filter combination. A mask was generated starting with the non-black pixels in each *HST* image. This mask was modified to blend the two images smoothly (Figure 26). Brightness adjustments were applied to match the images where they overlap. In addition to the large areas of blank data filled by the ESO images, areas were blended to fill in smaller gaps. After up-resampling the masked composite to the *HST* pixel size, the *HST* images were reincorporated to produce a flat, 16 bit version of each filter/color, cropped to the final orientation and size, $36,000 \times 36,000$ pixels (1.2 Gpix).

A.4. Composite, Balance Tonal Range Per Filter, and Apply Color

The next step was the creation of a color composite from the combined *HST* and ESO images, based on the initial prototypes with the *HST* data only. Brightness, contrast, and color balance adjustments were applied at this stage, both to the individual filter components and to the combined image. Masks were used to apply adjustments to localized areas with the goal of preserving detail and maximizing local contrast across the image (Figure 27).

A.5. Resize, Adjust Brightness, Contrast, and Color

At this point, the image was downsized by $2\times$ in each dimension, $18,000 \times 18,000$ pixels (309 Mpix), before applying further adjustments to improve brightness, contrast, and color. Again, masks were used to apply adjustments in selected regions to expand the overall tonal range. To further facilitate additional editing, the flat, 16 bit color composite was tiled into four pieces in a 2×2 array.

A.6. Retouch Cosmetic Artifacts

Our last steps of the process required some retouching and restoration. It is known that telescopes and cameras introduce certain well-known artifacts into astronomical images such as,

1. CCD saturation bleeding;
2. diffraction spikes;
3. residual cosmic rays;
4. internal reflections: primarily on brightest stars in the ground-based image, resulting from light reflecting, from filters and other optical elements within the instrument.

Most of these artifacts were removed from our Orion Nebula image using standard digital editing techniques, paying great attention to avoid changing the character of the underlying image (Figure 28).

A.7. Retile Mosaic, Final Adjustments, Sharpening, and High-pass Filter

After retouching, the four flattened tiles were reassembled into a full, flat mosaic. Some additional adjustments were applied, mostly to increase the overall contrast, enhancing detail

in the shadows while taking care not to lose detail in the highlights. A slight sharpening was applied to the final, flat image. Care was taken to do it in a minimal amount to avoid introducing visible sharpening artifacts. Finally, the overall contrast was slightly enhanced by inserting a copy of the image to which a moderate high-pass filter had been applied at 60% opacity (Figure 29).

REFERENCES

Aarnio, A. N., Stassun, K. G., & Matt, S. P. 2010, ApJ, 717, 93
Allard, F., Hauschildt, P. H., & Schwenke, D. 2000, ApJ, 540, 1005
Allard, F., Homeier, D., & Freytag, B. 2012, in ASP Conf. Ser. 448, 16th Cambridge Workshop on Cool Stars, Stellar Systems, ed. C. M. Johns-Krull, M. K. Browning, & A. A. West (San Francisco, CA: ASP), 91
Andersen, M., Meyer, M. R., Robberto, M., et al. 2011, A&A, 534, A10
Anderson, J. 2006, in The 2005 HST Calibration Workshop: Hubble After the Transition to Two-Gyro Mode, ed. A. M. Koekemoer, P. Goudfrooij, & L. L. Dressel (Greenbelt, MD: NASA), 11
Appenzeller, I., & Mundt, R. 1989, A&ARv, 1, 291
Bally, J., O'Dell, C. R., & McCaughrean, M. J. 2000, AJ, 119, 2919
Baraffe, I., Chabrier, G., Allard, F., & Hauschildt, P. H. 1998, A&A, 337, 403
Bertin, E., & Arnouts, S. 1996, A&AS, 117, 393
Briceño, C., Preibisch, T., Sherry, W. H., et al. 2007, in Protostars and Planets V, ed. B. Reipurth, D. Jewitt, & K. Keil (Tucson, AZ: Univ. Arizona Press), 345
Cardelli, J. A., Clayton, G. C., & Mathis, J. S. 1989, ApJ, 345, 245
Chabrier, G., Baraffe, I., Allard, F., & Hauschildt, P. 2000, ApJ, 542, 464
Da Rio, N., Robberto, M., Hillenbrand, L. A., Henning, T., & Stassun, K. G. 2012, ApJ, 748, 14
Da Rio, N., Robberto, M., Soderblom, D. R., et al. 2009, ApJS, 183, 261
Da Rio, N., Robberto, M., Soderblom, D. R., et al. 2010, ApJ, 722, 1092
Dolphin, A. E. 2000, PASP, 112, 1397
Eisner, J. A., Plambeck, R. L., Carpenter, J. M., et al. 2008, ApJ, 683, 304
Fruchter, A., Sosey, M., et al. 2009, The MultiDrizzle Handbook, Version 3.0 (Baltimore, MD: STScI), http://www.stsci.edu/hst/HST_overview/documents/multidrizzle/multidrizzle_cover.html
Fruchter, A. S., & Hook, R. N. 2002, PASP, 114, 144
Getman, K. V., Feigelson, E. D., Grosso, N., et al. 2005, ApJS, 160, 353
Gilliland, R. L. 2004, STScI ACS ISR 04-01
Gonzaga, S., et al. 2011, ACS Data Handbook, Version 6.0 (Baltimore, MD: STScI)
Güdel, M., Briggs, K. R., Montmerle, T., et al. 2008, Sci, 319, 309
Gullbring, E., Hartmann, L., Briceno, C., & Calvet, N. 1998, ApJ, 492, 323
Hauschildt, P. H., Allard, F., & Baron, E. 1999, ApJ, 512, 377
Henney, W. J., O'Dell, C. R., Zapata, L. A., et al. 2007, AJ, 133, 2192
Herbig, G. H., & Tendrup, D. M. 1986, ApJ, 307, 609
Herbst, W., Bailer-Jones, C. A. L., Mundt, R., et al. 2002, A&A, 396, 513
Herbst, W., Herbst, D. K., Grossman, E. J., & Weinstein, D. 1994, AJ, 108, 1906
Hester, J. J., & Desch, S. J. 2005, in ASP Conf. Ser. 341, Chondrites and the Protoplanetary Disk, ed. A. N. Krot, E. R. D. Scott, & B. Reipurth (San Francisco, CA: ASP), 107
Hillenbrand, L. A. 1997, AJ, 113, 1733 (H97)
Hillenbrand, L. A., & Carpenter, J. M. 2000, ApJ, 540, 236
Holden, E. 1882, Astronomical and Meteorological Observations Made at the U.S. Naval Observatory, 18, A1
Holtzman, J. A., Hester, J. J., Casertano, S., et al. 1995, PASP, 107, 156
Jeffries, R. D., Littlefair, S. P., Naylor, T., & Mayne, N. J. 2011, MNRAS, 418, 1948
Kaifu, N., Usuda, T., Hayashi, S. S., et al. 2000, PASJ, 52, 1
Lada, C. J., & Lada, E. A. 2003, ARA&A, 41, 57
Lada, C. J., Muench, A. A., Haisch, K. E., Jr., et al. 2000, AJ, 120, 3162
Looney, L. W., Tobin, J. J., & Fields, B. D. 2006, ApJ, 652, 1755
Lucas, P. W., & Roche, P. F. 2000, MNRAS, 314, 858
Lucas, P. W., Roche, P. F., & Tamura, M. 2005, MNRAS, 361, 211
Lucas, P. W., Weights, D. J., Roche, P. F., & Riddick, F. C. 2006, MNRAS, 373, L60
Luhman, K. L., Rieke, G. H., Young, E. T., et al. 2000, ApJ, 540, 1016
Maíz-Apellániz, J. 2004, PASP, 116, 859
Manara, C. F., Robberto, M., Da Rio, N., et al. 2012, ApJ, 755, 154
Maybhate, A., et al. 2010, ACS Instrument Handbook, Version 9.0 (Baltimore, MD: STScI), http://documents.stsci.edu/hst/acs/documents/handbooks/cycle18/cover.html
McCaughrean, M. J., & O'Dell, C. R. 1996, AJ, 111, 1977

McMaster, Biretta, et al. 2008, WFPC2 Instrument Handbook, Version 10.0 (Baltimore, MD: STScI), http://documents.stsci.edu/hst/wfpc2/documents/handbooks/cycle17/wfpc2_cover.html
Menten, K. M., Reid, M. J., Forbrich, J., & Brunthaler, A. 2007, A&A, 474, 515
Meyer, M. R., Calvet, N., & Hillenbrand, L. A. 1997, AJ, 114, 288
Miotello, A., Robberto, M., Potenza, M. A. C., & Ricci, L. 2012, ApJ, 757, 78
Muench, A. A., Lada, E. A., & Lada, C. J. 2000, ApJ, 573, 366
O'Dell, C. R. 2001a, AJ, 122, 2662
O'Dell, C. R. 2001b, ARA&A, 39, 99
O'Dell, C. R., & Harris, J. A. 2010, AJ, 140, 985
O'Dell, C. R., & Henney, W. J. 2008, AJ, 136, 1566
O'Dell, C. R., Henney, W. J., Abel, N. P., Ferland, G. J., & Arthur, S. J. 2009, AJ, 137, 367
O'Dell, C. R., Muench, A., Smith, N., & Zapata, L. 2008, Handbook of Star Forming Regions, Volume I: The Northern Sky, ed. B. Reipurth (ASP Monograph Pub., Vol. 4; San Francisco, CA: ASP), 544
O'Dell, C. R., Poveda, A., Allen, C., & Robberto, M. 2005, ApJL, 633, L45
O'Dell, C. R., & Wen, Z. 1994, ApJ, 436, 194
O'Dell, C. R., & Wong, K. 1996, AJ, 111, 846
O'Dell, C. R., & Yusef-Zadeh, F. 2000, AJ, 120, 382
Osterbrock, D. E., Tran, H. D., & Veilleux, S. 1992, ApJ, 389, 305
Prisinzano, L., Micela, G., Flaccomio, E., et al. 2008, ApJ, 677, 401
Prosser, C. F., Stauffer, J. R., Hartmann, L., et al. 1994, ApJ, 421, 517

Pudritz, R. E. 2002, Sci, 295, 68
Reggiani, M., Robberto, M., Da Rio, N., et al. 2011, A&A, 534, A83
Ricci, L., Robberto, M., & Soderblom, D. R. 2008, AJ, 136, 2136
Riddick, F. C., Roche, P. F., & Lucas, P. W. 2007, MNRAS, 381, 1077
Riess, A., & Mack, J. 2004, Instrument Science Report ACS 2004-006, 12
Robberto, M., Ricci, L., Da Rio, N., & Soderblom, D. R. 2008, ApJL, 687, L83
Robberto, M., Soderblom, D. R., Scandariato, G., et al. 2010, AJ, 139, 950
Robberto, M., Song, J., Mora Carrillo, G., et al. 2004, ApJ, 606, 952
Scally, A., Clarke, C., & McCaughrean, M. J. 2005, MNRAS, 358, 742
Scandariato, G., Robberto, M., Pagano, I., & Hillenbrand, L. A. 2011, A&A, 533, A38
Sirianni, M., Jee, M. J., Benítez, N., et al. 2005, PASP, 117, 1049
Skrutskie, M. F., Cutri, R. M., Stiening, R., et al. 2006, AJ, 131, 1163
Slesnick, C. L., Hillenbrand, L. A., & Carpenter, J. M. 2004, ApJ, 610, 1045
Stassun, K. G., Mathieu, R. D., Mazeh, T., & Vrba, F. J. 1999, AJ, 117, 2941
Thatte, D., Dahlen, T., et al. 2009, NICMOS Data Handbook, Version 8.0 (Baltimore, MD: STScI), http://documents.stsci.edu/hst/nicmos/documents/handbooks/v8/NICMOS_cyc15_ihb.pdf
van Dokkum, P. G. 2001, PASP, 113, 1420
Walsh, J. R., Freudling, W., Pirzkal, N., & Pasquali, A. 2003, ST-ECF Instrument Science Report ACS 2003-012, 1, 23 pp
Williams, J. P., & Gaidos, E. 2007, ApJL, 663, L33